Efficient generation of geodesic random fields in finite elements with application to shell buckling

Sander van den Broek[a], Eelco Jansen[b], Raimund Rolfes[a]

[a] *Leibniz University Hannover, Germany*
[b] *Rotterdam University of Applied Sciences, the Netherlands*

Abstract

Structures contain inherent deviations from idealized geometry and material properties. Quantifying the effects of such random variations is of interest when determining the reliability and robustness of a structure. Generating fields that follow complex shapes is not trivial. Generating random fields on simple shapes such as a cylinder can be done using series-expansion methods or analytically computed distances as input for a decomposition approach. Generating geodesic random fields on a mesh representing complex geometric shapes using these approaches is very complex or not possible. This paper presents a generalized approach to generating geodesic random fields representing variations in a finite element setting. Geodesic distances represent the shortest path between points within a volume or surface. Computing geodesic distances of structural points is achieved by solving the heat equation using normalized heat gradients originating from every node within the structure. Any element (bar, beam, shell, or solid) can be used as long as it can solve potential flow problems in the finite element program. Variations of the approach are discussed to generate fields with defined similarities or fields that show asymmetric behavior. A numerical example of a gyroid structure demonstrates the effect of using geodesic distances in field generation compared to Euclidean distances. An anisotropic cylinder with varying Young's modulus and thickness is taken from literature to verify the implementation. Variations of the approach are analyzed using a composite cylinder in which fiber angles are varied. Although the focus of this paper is thin-walled structures, the approach works for all types of finite element structures and elements.

Keywords: Geodesic Length, Heat Method, Random Field, FEM

1. Introduction

How a structure performs under loads depends on many parameters such as geometry, material properties, and the direction and magnitude of applied loads. These parameters are often considered constant and known, but in reality, they vary and introduce an element of uncertainty in structural analysis. As structures become more efficient and lightweight, the behavior of these uncertainties and their effect becomes more important.

Stochastic analysis of finite element problems has been around for many years [1, 2, 3, 4]. It is possible to model the effects of spatially varying material properties or thickness variations in thin-walled structures using these approaches. Applying imperfections is done by assigning a randomly generated value to the local coordinates within a structure. This field of values in space is often referred to as a *random field* or, less commonly, *stochastic field*.

Random field values at different points inside the spatial domain are correlated; if the correlations are positively-valued, points close to each other tend to have similar field values. Correlation between points on a field is generally a function of the distance between points, decreasing as the distance increases. The correlation of points in space can be defined using a correlation function, which goes from 1 to 0 as a function of distance and possibly other parameters. When the covariance between the pair $(\mathbf{x}, \mathbf{y})$ only depends on the difference $(\mathbf{x}-\mathbf{y})$, the field is considered *weakly homogeneous*. Similarly, the correlation between points might have a directional dependency. When the relationship between distance and correlation is the same irrespective of direction, the covariance is only a function of the magnitude $||\mathbf{x}-\mathbf{y}||$. Such a field is *isotropic*. Conversely, if there is a directional dependency, the field is *anisotropic*.

What these correlations look like in actual structures is a topic of ongoing research. Recent work has been done to find these patterns experimentally using coupon testing [5, 6, 7]. Investigating the spatial correlation of random variations in material properties in such a manner has many challenges. Not only do many samples have to be tested to gain relevant results, but these results might also only be valid for a specific production process and geometry. Using a different batch of material or having different environmental conditions can affect these variations.

Therefore, a promising method to gain statistical information on structures is to use non-destructive investigation (NDI). Applying such methods to composite structures makes it possible to gain information on the void content, fiber alignment, fiber volume fraction, and other parameters using ultrasonic and infrared thermography [8, 9, 10].

The information gained using these methods could potentially be used to map the correlation function of a structure more accurately.

Many approaches exist to generate and apply random fields [11, 12, 13, 14]. A distinction can be made between methods that define the values of fields as a continuous function and those that discretize the field and evaluate values at specific locations.

Continuous methods represent the field through a sum of functions. Such a sum can be composed of a series of orthogonal functions, often done through a Karhunen-Loéve (KL) expansion [4]. KL expansions require solving the Fredholm integral, which is only possible analytically for a limited set of correlation functions and geometries [15, 2]. Other geometries and correlation functions require a numerical solution to solve the eigenvalues and eigenfunctions of the Fredholm integral [16]. Alternatively, fields can be represented using a Fourier series [17] in which the Fourier coefficients and phase shifts match a desired spectral density.

Discrete approaches define values at discrete points within the domain, such as integration points, nodes, or element centers. This can be done through decomposition of the covariance matrix [18], discretized fast Fourier series [19], and local average subdivision [20], among others. These discretized values can then be interpolated among the field using shape functions [21], optimal linear estimation (OLE) [22], or spatial averaging [23].

Through the use of a correlation function and statistical properties, the stochastic response of a structure to random variations can be quantified. This can be used to design under uncertainty [24, 25], simulating the effects or random geometric imperfections on the ultimate load [26, 27], geometric imperfections affecting stability [28, 29, 30, 31, 32, 33, 34, 35, 36], effects fiber angle misalignments have on stability [37, 38]. Some authors have also analyzed the effects of material property variations [39] or combined material and geometry variations [40, 41, 42, 43]. Teixeira and Soares [44] investigated using random fields to study the effects of corrosion on the ultimate strength of plates. Recent work by the authors has analyzed the effects local thickness deviations can have on the fatigue life of a 3D printed component [45]. Analysis of soil mechanics is also done, where random variations in soil properties are represented using random fields [46, 47, 48, 49, 50]. Recent work by Zhang et al. [51] used an information-theoretic model to ensure non-Gaussianity of the random field. They used this to perturb the mesh while ensuring that faces do not intersect each other.

Fields generated in most of the previously mentioned analyses are generated and applied on thin-walled structures such as a flat panel or a cylindrical shell. For those structures, computing distances between points using coordinate transformations is straightforward. Though this works well for specific structures, this is not possible or trivial for most structures. Generating fields on domains with a concave surface, such as thin-walled structures containing curvature or a volume with a concave surface, necessitates a different approach. Using the Euclidean distance in computing the correlation will result in significant deviations from the intended correlation matrix unless the correlation length is short compared to the curvature of the structure.

A better approach is to use geodesic distance, which is the distance on the surface or within the volume of the structure. Computing shortest distances between points is a classic problem in computational geometry and has many different approaches [52]. Using geodesic random fields in structural problems was recently discussed by Scarth et al. [53], where use was made of a mesh flattening "MMP" approach [54]. Within this approach, the shortest geodesic path between two points is found using a continuous Dijkstra-type approach. Within the Dijkstra algorithm [55], the shortest path between two points is found by slowly expanding out from the origin point. This approach can give accurate results for the geodesic length but at a high computational cost. The order of operations is $O(n^2)$, which can cause this approach to become unfeasible for larger structures.

Recent work by Feng et al. [56], Liang et al. [57] tried a different approach using a machine-learning powered isometric feature mapping algorithm to reduce the dimension of the geodesic problem after flattening the geodesic problem to a problem in 2D Euclidean space. The geodesic distance can then be recovered using traditional methods like the classic Dijkstra algorithm. Limitations in this approach do exist. The approach does not work for all shapes and cannot easily be used for non-homogeneous and anisotropic random fields. The approach in the current form is also not suitable for recovering geodesic distances in non-shell elements.

Previously discussed approaches to computing the geodesic distances have limitations in suitable geometry. Methods are generally incompatible with higher-order or non-surface elements and not capable of computing anisotropic and non-stationary random fields. Scaling of operations also limits many approaches from being used effectively in generating random fields. The work presented in this paper discusses a computationally efficient way of computing distances in finite elements and using those to generate random fields. Based on the method presented by Crane [58] it is capable of computing geodesic distances using shell , beam and volume elements. Instead of using mesh flattening, the approach uses principles of heat conduction first to find the path of the shortest distance using the heat gradient and then solve the Poisson equation to recover the geodesic distance. Solving the Poisson equation can be done by pre-factoring the sparse equations, requiring minimal computational time to solve the distances between all points in a field. Geodesic distances computed through the geodesic heat method in finite elements are used to compute the autocorrelation matrix of a field encompassing the domain of the finite element model. Decomposing the autocorrelation matrix makes it possible to generate random fields with a designated correlation through a simple matrix-vector multiplication. Unlike many methods found in literature, this approach works for any complex geometry

and element type and does not make assumptions about the geometry of a structure.

Novel variations of the approach can allow for more accurate models for a class of engineering problems. Using the geodesic heat approach makes anisotropy in random fields possible through anisotropic heat conductivity. Another variation discussed is an approach to creating similar fields, which can be used in layered structures or coupled parameters.

2. Methodology

Random fields in this study are randomly generated patterns, but values are still correlated with each other. The correlation between the field values at two different points depends on the distance between the points for stationary fields. Generating random fields requires the desired autocorrelation to be given as an input. Functions used to determine the autocorrelation between points usually vary only with the distance between points. Not all functions can be used, as the autocorrelation matrix has to be positive definite. Correlation functions must satisfy Bochner's theorem, which states that functions must be symmetric, non-negative definite, and bounded in variation [14, sec. 3.6.3]. For correlation functions that only depend purely on distance, Bochner's theorem is equivalent to having a non-negative integrable spectral density (the integrability ensures a bounded variation).

When considering correlation functions on geodesic surfaces, it is essential to note that correlation functions that satisfy Bochner's theorem using Euclidean distances may not satisfy the theorem when using geodesic distances [59, 60, 61]. In general, the admissibility of a covariance function must be checked before being used on geometry or type of distance. Not doing so could potentially lead to non-positive-definite matrices [62, post. 2.10]. Issues were not encountered in the examples discussed in this paper but could arise in other shapes or with other types of correlation functions.

Two functions often found in literature (e.g. [4, 63, 64]) are the exponential type

$$\rho = e^{\frac{-L}{L_c}}, \tag{1}$$

and the square exponential function

$$\rho = e^{\frac{-L^2}{L_c^2}}, \tag{2}$$

where ρ is the defined correlation between two points, L is the distance between points, and L_c is the correlation length. The correlation functions decrease from 1 to 0 as distance increases. The speed of which depends on the function used and the correlation length. The correlation function of eq. (1) decreases slower than that of eq. (2). The way that the correlation evolves with distance can be related to a spectral density function using the Wiener-Khinchin theorem [65, 11].

2.1. Calculation of geodesic lengths

Geodesic distances are calculated using an implementation of Keenan Crane's heat method [58]. Crane's approach is an extension of the work done by Varadhan [66], which sought to find an elegant solution to the heat equation. Distances from a point a to other points are calculated by calculating a normalized heat gradient from heat applied at point a, followed by solving the Laplacian to find the distance between points. Numerically this approach is fast and can be pre-factored for large systems.

Initially developed in a computational geometry framework, this paper reformulates the approach by Crane et al. into a finite element environment. Using potential flow tools commonly found in finite element solvers to solve thermal problems, the approach to computing geodesic distances is straightforward to implement in many other finite element solvers.

The examples used in this paper utilize an implementation that has been developed using the library of potential flow elements already built into DIANA [67], a commercial finite element solver.

The product of the calculation is to generate a length array $\mathbf{L} \in \mathbb{R}^{n\times n}$, with n the number of points in the array, in this case, nodes of the structure. The length array should be symmetric as distances are not direction-dependent. Meaning that $L_{a,b} = L_{b,a}$, the diagonal is filled with zeros. Resulting in an array in the form of

$$\mathbf{L} = \begin{bmatrix} L_{a,a}=0 & L_{a,b} & \cdots & L_{a,n} \\ L_{b,a} & 0 & \cdots & L_{b,n} \\ \vdots & & \ddots & \\ L_{n,a} & L_{n,b} & \cdots & 0. \end{bmatrix} \tag{3}$$

As described in [67, sec. 81.4] and [68, ch. 12] a heat conduction problem can be formulated using finite elements as

$$\mathbf{K}\boldsymbol{\phi}_i + \mathbf{C}\dot{\boldsymbol{\phi}}_i = \mathbf{q}_i, \tag{4}$$

where $\mathbf{K}$ is the conductivity matrix, $\mathbf{C}$ is the capacity matrix and $\mathbf{q}_i$ is a combination of external heat flux, heat generation and boundary convection vectors. The vector quantity $\boldsymbol{\phi}$ is the potential term and equals the temperature within a thermal problem.

Computing the distance at every point i of a mesh requires the right-hand side to be updated n times. Every calculation uses a different external heat flux $\mathbf{q}_i$, where heat is added to the structure at a single node using unit values for heat conductivity, heat capacity, and external heat flux. Combining all of these into one expression results in

$$\mathbf{K}\boldsymbol{\Phi} + \mathbf{C}\dot{\boldsymbol{\Phi}} = \mathbf{Q}, \tag{5}$$

where the matrix $\mathbf{Q}$ can be thought of as an identity matrix $\mathbf{I}_n$, and $\boldsymbol{\Phi}$ contains the potential terms associated with all i points.

In order to calculate the distances, the heat conduction problem has to be solved, meaning that a hypothetical heat

source is added to the structure. This is done using explicit Euler forward time integration. Hypothetically the results should become exact when the time step $t \to 0$. In practice, however, small time steps lead to numerical instability. The optimum time step, therefore, has to be given as input. The optimum value for the time step depends on the mesh. Crane et al. [58] recommend $t = \delta^2$, where δ is the mean edge length of the mesh analyzed. When SI units are used in the analysis t is in seconds and δ in meters.

Through numerical integration eq. (4) can be rewritten into the form of

$$\mathbf{K}^*\boldsymbol{\phi}^* = \mathbf{Q}^*, \tag{6}$$

where $\mathbf{K}^*$, $\boldsymbol{\phi}^*$ and $\mathbf{Q}^*$ are the effective matrix, nodal potential and fluxes [67, eqn. 81.18].

The solution $\boldsymbol{\phi}^*$ provides a thermal flux of the structure originating from the node specified in $\mathbf{Q}^*$. Normalizing this gradient is carried out by removing the magnitude of the flux

$$\mathbf{X}_a = -\frac{\nabla\boldsymbol{\phi}_a}{|\nabla\boldsymbol{\phi}_a|}, \tag{7}$$

which is unique for every node a. By integrating this normalized flux over the elements using the gradient of the element shape function N[1]

$$\mathbf{d}_a = \int\int \mathbf{X}_a \nabla N(\xi,\eta)\mathrm{d}\xi\mathrm{d}\eta, \tag{8}$$

a vector $\mathbf{d}_a$ containing incremental distances between nodes is generated.

Using the vector $\mathbf{d}$ it is now possible to easily calculate the distance vector for all the points from node a as

$$\mathbf{s}_a = (\mathbf{K}^*)^{-1}\mathbf{d}_a. \tag{9}$$

Note that the same inverted matrix used to solve eq. (6) is used to solve this equation. As mentioned by Crane the solution for eq. (9) is only unique up to an additive constant. By adding the minimum value of the calculated length vector the distances can be calculated.

The performance of the approach scales very well with the size of the model. Pre-factoring of the left-hand side of the equation scales sub quadratically, and even close to linearly [69]. Solving distances to other points scales linearly with the number of points of the model. Recent work on geodesic distances computed on shell elements by Scarth et al. [53] used a method first proposed by Mitchell et al. [54]. The exact method does not allow pre-computation and scales with $O(n^2 \log n)$, where n is the number of nodes in the model.

A performance comparison done between these approaches by Crane et al. [69] showed that for a 1.6M triangle Ramses model, the computation of distances from one point is approximately four times faster using the heat method, even with pre-factoring included. Different distances from another point of the model can be solved almost 200 times faster than the exact algorithm, with a mean error of only 0.24%. As generating an autocorrelation matrix requires the distances from all points to each other, the additional speedup of the implementation becomes essential for larger models.

This approach works on solid, shell, truss and beam elements as long as they are capable of solving potential flow problems.

2.2. Generation of random fields

Discretized random fields consist of points representing randomly generated variables in space. Values within the field have a predefined correlation to each other.

Correlation between two random variables X and Y is defined mathematically as [70, ch. 10]

$$\rho(X,Y) = \frac{\mathrm{Cov}(X,Y)}{\sqrt{\mathrm{Var}(X)\mathrm{Var}(Y)}} = \frac{E[(X-E[X])(Y-E[Y])]}{\sqrt{\mathrm{Var}(X)\mathrm{Var}(Y)}}, \tag{10}$$

where E is the expectation operator. If we define that X and Y have a mean value of zero, and a unit variance, the equation can be simplified to

$$\rho(X,Y) = \mathrm{E}(XY). \tag{11}$$

If X and Y are uncorrelated to each other; $\mathrm{E}(XY) = \rho = 0$. If they are correlated $\rho \in [-1,0)\cup(0,1]$.

Gathering all points of a random field into a vector $\mathbf{z}$ the correlation between points in an uncorrelated random field is $\rho(X_i, Y_j) = \mathrm{E}(X_i Y_j) = \delta_{i,j}$, meaning that the correlation matrix $\mathbf{R} = \mathbf{I}$. When values are correlated to each other, the off-diagonal entries of the array become populated with values between 0-1.

To generate correlated random fields using uncorrelated random Gaussian vectors, a a lower triangular matrix $\mathbf{T}$ is introduced to map uncorrelated values into correlated values as

$$\mathbf{z} = \mathbf{T}\mathbf{x}, \tag{12}$$

with $\mathbf{z}$ being a correlated Gaussian random vector with zero mean and unit variance. Vector $\mathbf{x}$ is an uncorrelated Gaussian random vector with zero mean and unit variance. Substituting eq. (12) into the simplified definition of correlation of eq. (11) the correlation matrix can be rewritten as

$$\begin{aligned}\rho(\mathbf{z}_1,\mathbf{z}_2) = \mathbf{R} &= \mathrm{E}(\mathbf{z_1}\mathbf{z_2}^T)\\ &= \mathrm{E}(\mathbf{T}\mathbf{x_1}\mathbf{x_2}^T\mathbf{T}^T)\\ &= \mathbf{T}\,\mathrm{E}(\mathbf{x_1}\mathbf{x_2}^T)\mathbf{T}^T\\ &= \mathbf{T}\,\mathbf{I}\,\mathbf{T}^T\\ &= \mathbf{T}\,\mathbf{T}^T\end{aligned} \tag{13}$$

Meaning that the correlation matrix can be written as

$$\rho(\mathbf{z}_1,\mathbf{z}_2) = \mathbf{R} = \mathbf{T}\,\mathbf{T}^T, \tag{14}$$

where $\mathbf{R}$ can be given as an input, giving the correlation between points as an input, using, for instance, eqs. (1) and (2),

[1] Using a 2D shell element as an example.

which define an input correlation as a function of the distance between points. Distances from the length array computed in the previous section can be used to compute values in the correlation matrix. Doing this will lead to an array in the form of

$$\mathbf{R} = \begin{bmatrix} 1 & \rho_{1,2} & \dots & \rho_{1,n} \\ \rho_{2,1} & 1 & \dots & \rho_{2,n} \\ \vdots & & \ddots & \\ \rho_{n,1} & \rho_{n,2} & \dots & 1 \end{bmatrix} = \mathbf{T}\,\mathbf{T}^T. \tag{15}$$

There are different ways to factorize the correlation matrix $\mathbf{R}$ into an upper and lower triangular matrix. The two most common approaches are using Cholesky decomposition and using eigenmode decomposition. For larger systems, eigenmode decomposition has fewer numerical issues and can also be done using a limited number of modes without significant loss of accuracy [71]. Another advantage is, although theoretically, a symmetric positive definite matrix only has positive eigenvalues. Numerical issues can cause these eigenvalues to become very small negative values. This can also be corrected by manually setting these eigenvalues to zero [72].

Eigenvalue decomposition can be done by calculating the eigenvalues and eigenvectors of the correlation matrix as

$$\mathbf{R} = \mathbf{Q}\mathbf{\Lambda}\mathbf{Q}, \tag{16}$$

where $\mathbf{Q}$ is an array containing the eigenvectors of the array, and $\mathbf{\Lambda}$ is a diagonal array with the squared eigenvalues. Taking the square root of the diagonal array, $\hat{\mathbf{\Lambda}} = \text{diag}(\sqrt{\lambda})$ eq. (16) can be rewritten as

$$\mathbf{R} = \mathbf{Q}\hat{\mathbf{\Lambda}}\hat{\mathbf{\Lambda}}\mathbf{Q} = \mathbf{T}\,\mathbf{T}^T \rightarrow \mathbf{T} = \mathbf{Q}\hat{\mathbf{\Lambda}}. \tag{17}$$

For a large number of random fields, this decomposition only has to be done once. To calculate more fields, this decomposed matrix simply has to be multiplied by an uncorrelated zero mean unit variance Gaussian random vector using eq. (12). An overview of the entire procedure to generate geodesic random fields is shown in algorithm 1.

Fields generated in this manner have unit variance and zero-mean. Scaling of the field is done when it is applied to a structural parameter in the finite element model. Alternatively, fields can be generated with a specified variance by factorizing the covariance matrix ($\mathbf{C} = \sigma^2\mathbf{R}$) the same way the correlation matrix $\mathbf{R}$ was factorized in eq. (13).

Examples in section 4 utilize shell elements. Using shell elements is useful in demonstrating the effects of geodesic distances. The approach described in section 2 is not limited to shell elements. Figure 1 shows a distance calculation and random field generated on a 3D tetrahedral model of a compressor blisk.

2.2.1. Applying fields on a structure

The implementation used within this paper utilizes an identical mesh for the random field and the structure. Using the element's shape function, scalar quantities, such as Young's modulus, thickness, or material orientation (angle), can easily be mapped from nodes to integration points. The value of these quantities is computed as

$$a_i = a_\mu + z_i a_\sigma, \tag{18}$$

in which a_i is a scalar quantity used in the model (such as thickness or Young's modulus), a_μ the mean value of a, z_i the value of the random field, a_σ the standard deviation of a, all evaluated at point i.

Geometric imperfections are not a scalar quantity, as they require a direction for the imperfection to act in. Assuming the structure is modeled using shell elements, geometric imperfections can be defined as a translation of nodes normal to its surface. Finding the normal direction of a shell is done by first finding the tangential components of the element coordinate system (ξ, η) in the global coordinate system. Partial derivatives of shape function have the property of transforming coordinates into vectors oriented in the derivative direction. The direction normal to the surface is found by computing the cross product of the shape function derivatives in the in-plane direction. With this in mind, the unit normal vector of point i on element j is

$$\mathbf{n_i} = \frac{\mathbf{X}_j \frac{\partial N(\xi,\eta)}{\partial \xi} \times \mathbf{X}_j \frac{\partial N(\xi,\eta)}{\partial \eta}}{\left| \mathbf{X}_j \frac{\partial N(\xi,\eta)}{\partial \xi} \times \mathbf{X}_j \frac{\partial N(\xi,\eta)}{\partial \eta} \right|}, \tag{19}$$

where ξ, η are the element coordinates as shown in fig. 2, $\mathbf{X}_j$ are node coordinates of element j. As an example, to calculate the normal of node 1 of a quadratic shell element shown in fig. 2 the values $\eta = \xi = -1$ are used. $\mathbf{X}_j$ being an array of the coordinates of all the nodes of the element. Nodes which are part of multiple elements take the average normal calculated using all elements.

Algorithm 1: Heat method for finite element random fields

input : Mesh, t
output: n samples of $\mathbf{z}$

Compute $\mathbf{K}^*$ using t ; `/* Distance calculation */`
Solve the Poisson equation for $\boldsymbol{\phi}^*$ (eq. (6));
Normalize flux to obtain $\mathbf{X}_a$ (eq. (7)) ;
Compute incremental distances $\mathbf{d}_a$ (eq. (8)) ;
for *Every point a in mesh* **do**
    Compute distances $\mathbf{s}_a$ from point a (eq. (9)) ;
    Subtract minimum distance $\mathbf{s}_a = \mathbf{s}_a$ - min($\mathbf{s}_a$) ;
Assemble all distances $\mathbf{s}_a$ into a distance array $\mathbf{L}$;
Force symmetry of $\mathbf{L}$, $\mathbf{L} = 0.5(\mathbf{L} + \mathbf{L}^\intercal)$;
Compute $\mathbf{R}$ using $\mathbf{L}$ (e.g. eqs. (1) and (2)) ; `/* RF generation */`
Decompose $\mathbf{R}$ into triangular form $\mathbf{T}$ (eq. (14)) ;
for $i = 1{:}n$ **do**
    $\mathbf{z}_i = \mathbf{T}\mathbf{x}_i$ (eq. (12))

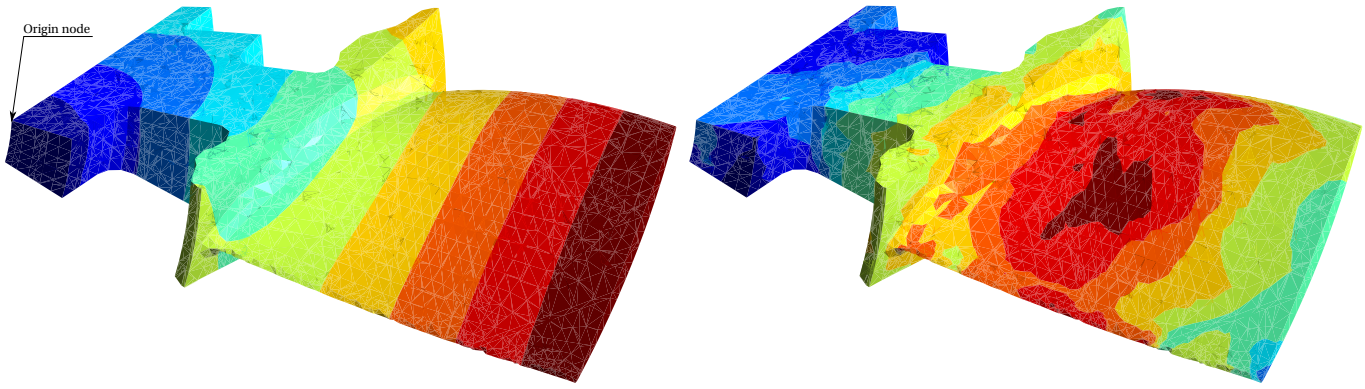

(a) Distance calculation

(b) Example of random field

Figure 1: Example of geodesic distance calculation and random field generation on a tetrahedral mesh model of a compressor blisk, model courtesy of authors of [73]

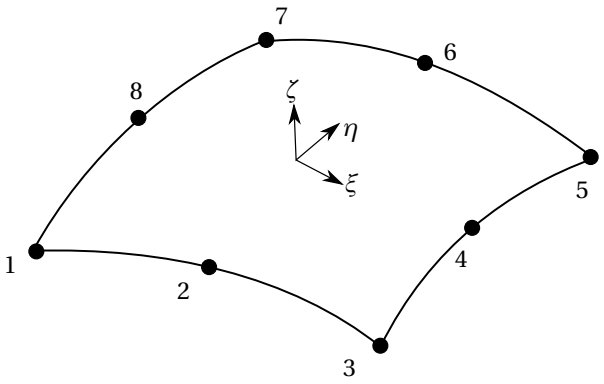

Figure 2: Element numbering and coordinates of a quadratic shell element

This approach for geometric imperfection only works on structures that consist of one surface. Applying geometric imperfections generated by random fields on structures consisting of multiple surfaces (such as an I-beam) is more involved but can be done by decomposing the deformation into local and global components [74, 75].

2.3. Extensions of random field generation approach

What has been presented up to now can be used to generate isotropic homogeneous random fields that are uncorrelated with each other. However, certain structural problems could benefit from extensions to this approach, allowing for better modeling of certain variations. Therefore, within this section two extensions are introduced which can make it possible to generate more realistic imperfections in, for instance, layered orthotropic structures such as composites.

2.3.1. Generation of correlated random fields

In some analyses, the imperfections correlate with each other. In those cases, it is of interest to generate random fields which have a pre-determined inter-correlation. An example can be the different lamina in a composite structure. In these structures, imperfections can have different sources. Errors due to initial fiber placement would be independent of each other in every layer, but errors due to curing would affect the structure more uniformly. One way to model these coupled imperfection patterns is to generate fields that are correlated with each other.

How to generate correlated random fields is very similar to the approach used to generate random fields in section 2.2. A correlation matrix defines the relationship between random fields. A series of n intercorrelated fields requires an $n \times n$ symmetric correlation matrix. The correlation between fields can be constant or can be neighbor dependent. It may be that neighboring layers in a composite structure are more correlated to each other than layers on the outer surface. The similarity between random fields is defined through a symmetric correlation matrix describing the similarity of fields generated in a grouping using

$$\mathbf{R} = \begin{bmatrix} 1 & \rho_{1,2} & \cdots & \rho_{1,n} \\ \rho_{2,1} & 1 & \cdots & \rho_{2,n} \\ \vdots & & \ddots & \\ \rho_{n,1} & \rho_{n,2} & \cdots & 1 \end{bmatrix} = \mathbf{T}\,\mathbf{T}^T \tag{20}$$

where n is the number of correlated random vectors. Decomposing this in the form shown in eq. (14) it is possible to create correlated random vectors as

$$\mathbf{Y} = \mathbf{T}\,\mathbf{X}, \tag{21}$$

where $\mathbf{Y}$ is an array with correlated random vectors as its columns, $\mathbf{X}$ a matrix with uncorrelated random vectors as its columns and $\mathbf{T}$ the decomposed matrix of eq. (15). Using these correlated random vectors, correlated random fields can be generated using eq. (12).

Section 4.3 discusses an example in which the correlation of fiber misalignments through different layers of a composite shell are analyzed. Intercorrelated, through-thickness varying and independent fields are compared for their relative influence on structural buckling.

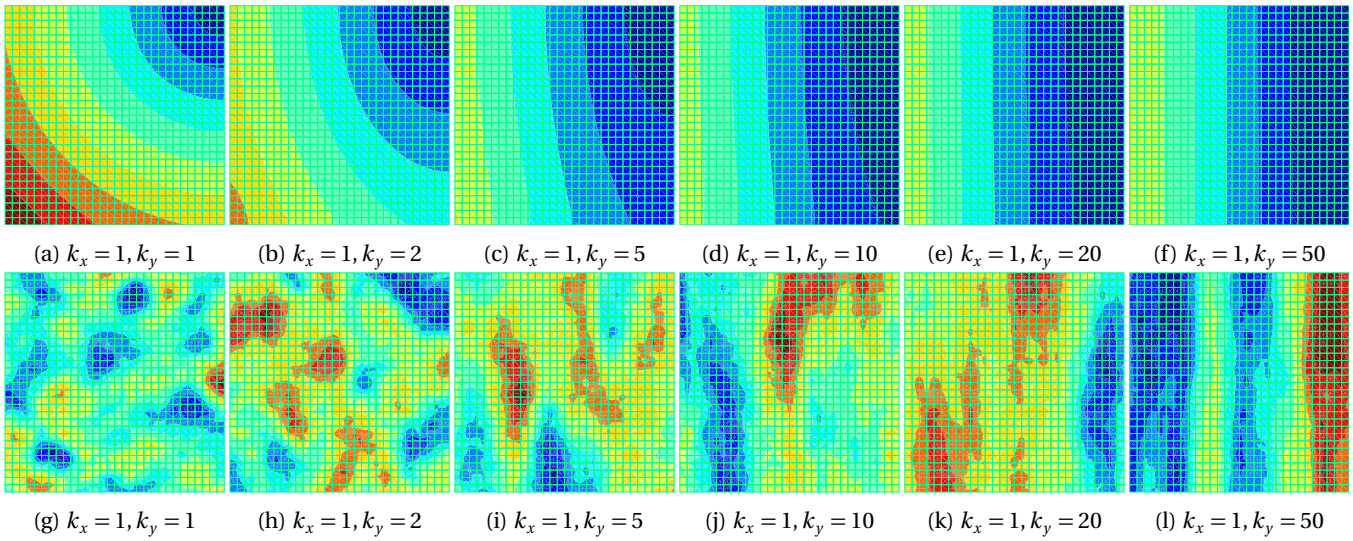

(a) $k_x = 1, k_y = 1$ (b) $k_x = 1, k_y = 2$ (c) $k_x = 1, k_y = 5$ (d) $k_x = 1, k_y = 10$ (e) $k_x = 1, k_y = 20$ (f) $k_x = 1, k_y = 50$

(g) $k_x = 1, k_y = 1$ (h) $k_x = 1, k_y = 2$ (i) $k_x = 1, k_y = 5$ (j) $k_x = 1, k_y = 10$ (k) $k_x = 1, k_y = 20$ (l) $k_x = 1, k_y = 50$

Figure 3: Pseudo-distances from the top right corner (a-f), and fields generated on a 10x10 m flat plate using a correlation length of 1 m and correlation function eq. (23) (g-l). Thermal conductivity is constant in the horizontal (x) direction and varies in the vertical (y) direction.

2.3.2. *Tailoring of thermal conductivity to generate asymmetric random fields*

The approach originally presented by Crane [58] utilizes a thermal capacity $C = 1\ \frac{\mathrm{J}}{\mathrm{K}}$ and thermal conductivity $k = 1\ \frac{\mathrm{W}}{\mathrm{m \cdot K}}$. When solving the heat equation, this converges to the geodesic length between points. Using anisotropic heat conductivity enables the generation of a metric in which points on the structure are connected through a scaled pseudo-distance. This concept was first studied by [76]. Introducing an anisotropic pseudo-distance to determine the correlation between points on a structure makes it possible to generate fields that show different correlation behavior in different axes, such as limiting variation in a particular direction while showing more in the other direction.

One approach often used in literature (e.g. [46, 53, 77]) is to define a correlation length per axis. For instance converting eqs. (1) and (2) to

$$\rho = e^{-\sqrt{\frac{L_x^2}{L_{c,x}^2} + \frac{L_y^2}{L_{c,y}^2}}}, \tag{22}$$

and the square exponential function

$$\rho = e^{-\left(\frac{L_x^2}{L_{c,x}^2} + \frac{L_y^2}{L_{c,y}^2}\right)}, \tag{23}$$

in which L_x and L_y are the x and y components of the distance between points, and $L_{c,x}$ and $L_{c,y}$ the correlation length in those directions.

Decomposing a distance to (local) coordinates is not a trivial task, except for simple geometries such as cylindrical shells and flat plates. Using the approach presented in this paper, it is possible to directly represent this asymmetric behavior by influencing the heat flow in the geodesic distance calculation.

The heat conductivity used in the geodesic distance calculation of section 2.1 is inversely proportional to the distance calculated. Assuming homogeneous orthotropic thermal properties, the correlation functions in eqs. (22) and (23) can be reproduced by implementing this orthotropy into the correlation lengths $L_{c,x}$ and $L_{c,y}$ as

$$L_{c,x} = a\, L_c, \tag{24}$$

$$L_{c,y} = b\, L_c. \tag{25}$$

where a and b are scaling parameters of the the thermal conductivity in the element's x and y directions

$$k_x = a\, k, \tag{26}$$

$$k_y = b\, k. \tag{27}$$

This effectively replaces the geodesic distance with a weighed pseudo distance, in which the effective correlation length is the product of the thermal conductivity and the axis-independent correlation length. Examples of distance and random fields generated using anisotropic thermal conductivity are shown in fig. 3. Increasing anisotropy is applied to the thermal properties resulting in increasing anisotropy in the random fields.

Orientation of the material can be defined in the global coordinate system or a local coordinate system. Local material orientation can be defined through a parametric equation or as a manual input to the nodes or centroid of elements. Material anisotropy in the heat conductivity used to compute pseudo-distances makes generating anisotropic random fields on complex geometry possible.

This approach can also generate non-homogeneous fields by varying the thermal conductivity at areas with different correlation behavior (e.g., seams and edges). Increasing the thermal conductivity in these areas can cause the variations to have a shorter correlation length than their surroundings. Decreasing thermal conductivity can cause the local variation to become more constant. The use of locally varying thermal conductivity is not further explored within this paper.

3. Analysis of accuracy and time step of geodesic distance calculation

Numerical algorithms should converge to an exact solution with increased refinement. In order to verify that the implementation described in section 2 complies with this paradigm, a number of analyses were performed. These analyses compared the computed geodesic distance and compared it to one obtained analytically. These studies were performed on a flat plate, cube, and cylindrical shell. For the sake of brevity, only the cylindrical shell is discussed in more detail.

3.1. Optimal time step and error of geodesic distance calculation

As mentioned by Crane [58] it is not trivial to find an optimal time step for geodesic length calculation. The ideal time step depends on the size, shape, and average edge length of the elements within a mesh. The geodesic calculation becomes more accurate with a finer mesh, while the ideal time step decreases with an increasing mesh size.

The error in distance calculation between the length arrays in the form of eq. (3) obtained analytically ($\mathbf{L}_A$) and numerically ($\mathbf{L}_N$) is calculated as

$$\boldsymbol{\epsilon} = \frac{\mathbf{L}_N - \mathbf{L}_A}{\mathbf{L}_A + \mathbf{I}}. \tag{28}$$

Array $\boldsymbol{\epsilon}$ contains all the relative errors between points in the model. Within the results shown here, the RMS value of the array entries is taken as a comparative measure. The RMS is defined as

$$\text{RMS Error} = \sqrt{\frac{\epsilon_{1,1}^2 + \epsilon_{2,1}^2 + \ldots + \epsilon_{n,1}^2 + \ldots + \epsilon_{n,n}^2}{n}} \tag{29}$$

where n is the number of nodes of the mesh.

3.1.1. Numerical example of distance calculation

Cylindrical shells are often found in many structures in engineering and are therefore of particular interest. Different discretizations are analyzed to find the optimal time step depending on the geometry. Discretizing a shell into m circumferential elements and n axial elements, nodes are located every $\alpha = \frac{360}{m}$ degrees on the circumference. Due to the discretization, the circumference of a meshed cylindrical shell is less than an analytical cylinder. Using the equation for a chord of a circle segment [78, sec. 3.8] $c = 2R\sin\frac{\alpha}{2}$. The perimeter of the geometry represented by the discrete mesh is therefore $d = 2mR\sin\frac{360}{m2}$ (in degrees). Results generated using the heat method are compared to the analytical solution

$$L_{a,b} = \sqrt{\left(2miR\sin\frac{360}{2m}\right)^2 + \left(\frac{jL}{n}\right)^2}, \tag{30}$$

in which i is the number of elements between nodes a and b in the circumferential direction. j is the number of elements between nodes a and b in the axial direction. A discretization of one of the analyzed cylinders can be found in fig. 4a, with an example of a distance calculation shown in fig. 4b.

3.1.2. Numerical results and trends

Figure 5 shows how the RMS error in distance calculation changes with differing time steps when analyzing a cylinder with radius $R = 1$ and length $L = 2$. The analyses show that the RMS error decreases with a decreasing time step up to a certain point. At this point, it rapidly increases or does not converge. Minimization of the time step does not occur when the time goes to zero. Analyses done by Crane et al. [69, App. A] show that as the time step goes towards the limit of zero, the computed distances become a combinatorial distance, e.g., the distance product computed converges to $L = x + y$ instead of $L = \sqrt{x^2 + y^2}$. Increasing the time-step smooths out the fluxes computed, smoothening the distances computed and reducing accuracy. The exact curves vary with the aspect ratio/model size, as shown in fig. 6. These are generated using a fixed radius of 1 m with a varying length between 1-3 m. Accuracy in the distance calculation improves with mesh size, as shown in fig. 6a.

Time steps in which the RMS error is minimized were computed using Brent's method [79]. The ideal time step for cylindrical shells was close ($R^2 = 0.947$) to

$$t = \delta^{1.7}, \tag{31}$$

where δ is the mesh's mean edge length. This relationship is a similar result to that recommended by Crane ($t = \delta^2$). Better fits were found with long polynomial expressions, but none of these expressions were accurate for different geometries. The recommendation of Crane is therefore a good starting point for meshes in general.

3.1.3. Anisotropic heat conduction

Utilizing pseudo-distances to create anisotropic fields was discussed in section 2.3.2. This section analyzes the pseudo-distances relationship to (scaled) distance. This is done by varying the conductivity ratios[2] $\frac{k_z}{k_{x,y}}$ of a cylindrical shell. Ratios ranging from 0.1 to 10 were computed and compared to the analytical result found by modifying eq. (30) to

$$L_{a,b} = \sqrt{\left(2miRk_{x,y}\sin\frac{360}{2m}\right)^2 + \left(\frac{jL}{nk_z}\right)^2}, \tag{32}$$

with k_z being the axial thermal conductivity and $k_{x,y}$ the thermal conductivity in the circumferential direction. Figure 7 shows the minimized RMS error for different conductivity ratios. These minimized errors were obtained using Brent's method. Results show that with an increasing anisotropy, the direct relationship with distance becomes unclear. Though not necessarily an issue for generating inhomogeneous random fields, this should nevertheless be considered when the correlation function is defined.

[2] z being the axial direction.

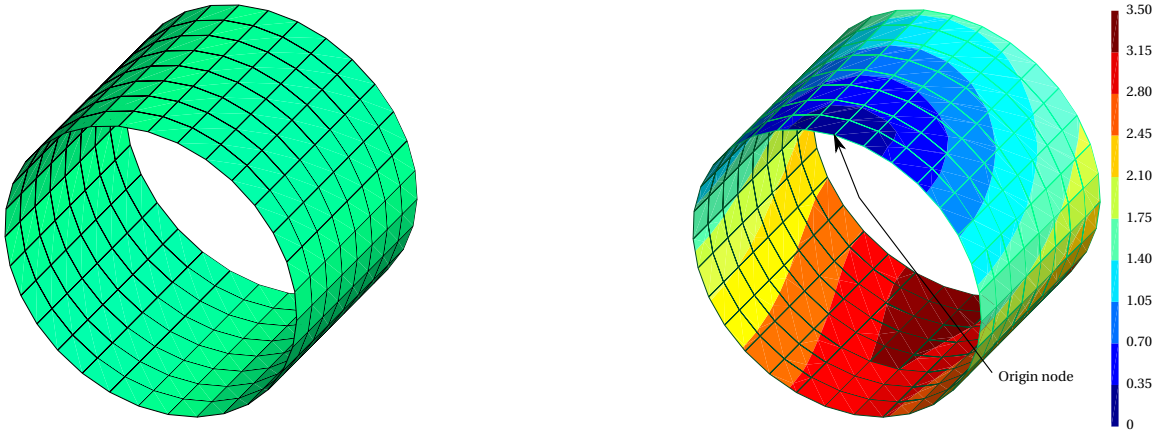

(a) Mesh

(b) Example of geodesic distance calculation from an origin node

Figure 4: Example of cylindrical shell mesh $R = 1, \quad L = 1.5, \quad \delta = 0.2$

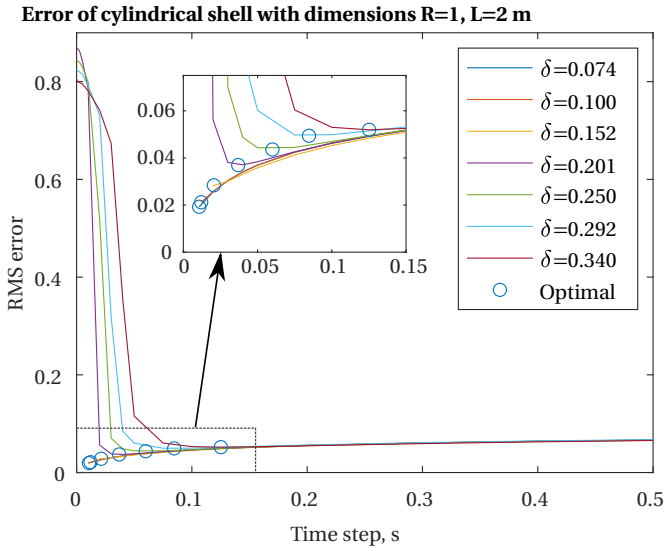

Figure 5: RMS error in distance calculation of a cylindrical shell using different mean element size δ and time steps

4. Numerical examples

A series of numerical analyses verify the implementation in Diana and demonstrate its use on structures, including how the extensions of section 2.3 can be used. Numerical analyses focus on cylindrical shells as these are easy to model, and using geodesic length can considerably influence results. In addition to this, cylindrical shells benefit from having many examples analyzed in detail in published literature.

Verification of the random field implementation is done by analyzing Young's modulus and thickness variations of an isotropic cylinder. Following this analysis, a cylindrical shell's geometric imperfections are analyzed and compared to those published in literature. A final numerical study is performed to analyze variations in the fiber angle of a composite cylindrical shell's buckling load.

The last part of the section demonstrates some other structures in which fields were generated, showing its use in more complex structures.

4.1. Gyroid structure

Gyroid structures are a form of a minimal surface first described by Schoen [80]. Minimal surfaces are surfaces for which the mean curvature equals zero. Gyroids can be described mathematically as a surface defined by

$$\sin x \cos y + \sin y \cos z + \sin z \cos x = 0. \tag{33}$$

Recent work showed that gyroid shapes are very strong porous structures that efficiently use space [81], and can be fabricated using additive manufacturing techniques. The effective strength of the structure is directly related to the wall thickness, and the size of the periodic gyroids [82, 83, 84]. Additive manufacturing techniques can cause local variations in thickness. Within the current analysis, fictional variations in thickness are introduced, where the x-displacement at the loaded edge $y = 0$ is measured. Comparing the stochastic response of the structure with the ran-

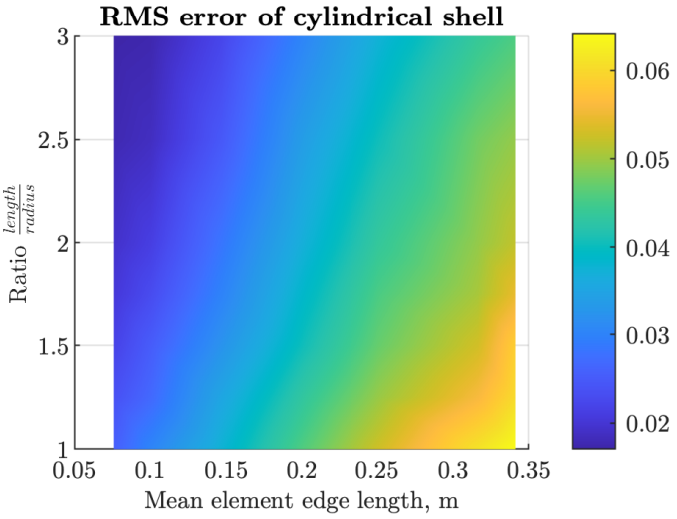

(a) Lowest RMS error found in the distance computation of cylindrical shell

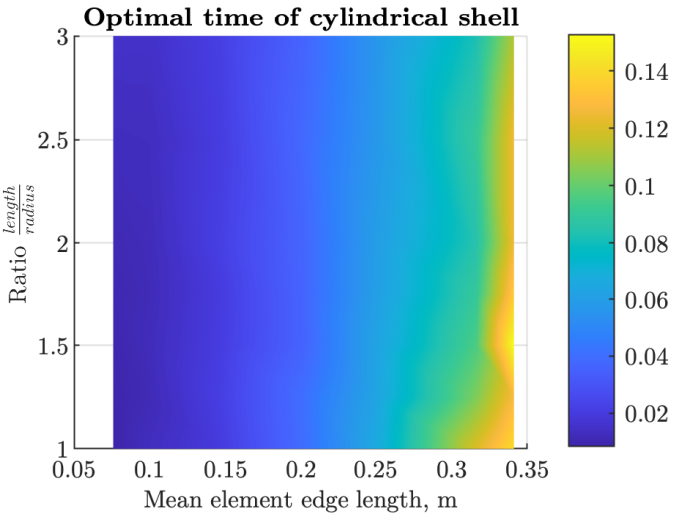

(b) Time step in which the lowest RMS distance error is achieved, s

Figure 6: RMS geodesic distance error minimization achieved and the time steps in which it is achieved over a variety of element sizes and geometric ratios

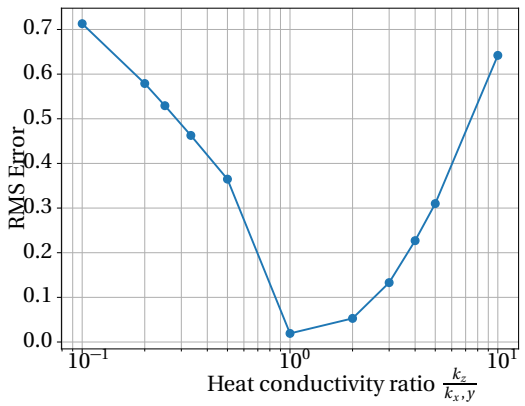

Figure 7: RMS error of best time step found of various conductivity ratios within a cylindrical shell of R=1, L=2

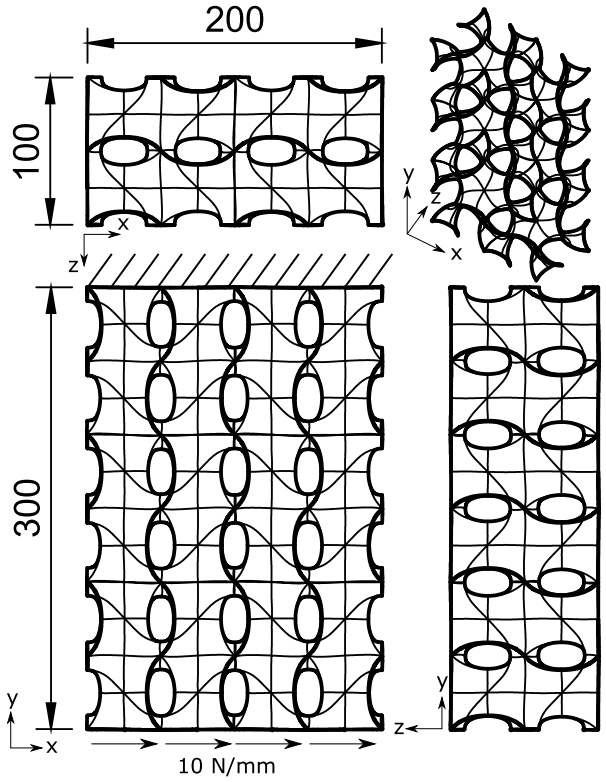

Figure 8: Gyroid geometry, boundary conditions, and load. Dimensions in mm

dom field-generated imperfections using geodesic and Euclidean distances gives an impression of the relative influence both measures have.

4.1.1. Numerical analysis

A series of gyroids with 100 mm sides are assembled in a 2x3 configuration as shown in fig. 8. The model is discretized into 8558 analytically integrated triangular shell elements. Mesh convergence is done to check if the end displacement converges with the chosen refinement. A shear load of 10 N/mm is applied to the edges where y=0. Displacements of nodes located at $y = 0$ are tied together, making them equal on one edge of the gyroids. Clamped boundary conditions are applied to the edge where $y = 300$ mm. Numerical modeling of the structure is done using bilinear triangular shell elements. Thickness varies through a Gaussian distributed random field. Table 1 lists the parameters of the random field and the material properties used in the analyses. Thickness variations in the shell are applied as scalar variations on the shell element using eq. (18). One thousand samples are generated for both types of distance calculations. A 100 mm correlation length is used as it is of a similar order of magnitude as the structure. Very small or large correlation lengths will not show as much of a distinctive difference. In theory, a Gaussian distribution can result in a locally negative thickness that would not be physically possible. However, the chance of this happening with a standard deviation of $0.1t$ is negligible. Computing the probability using

Property	Value
E	210 GPa
ν	0.3
Thickness	Gaussian random field: $\mu = 0.5$ mm $\sigma = 0.05$ mm (CoV 10%) $L_c = 100$ mm

Table 1: Deterministic and statistical properties of gyroid structure

	μ, mm	σ, mm	CoV
Geodesic	1.626	0.134	8.24%
Euclidean	1.617	0.158	9.78%
Relative difference	-0.5%	18.1%	18.7%

Table 2: Statistical properties of analyses of the x-direction displacement of the loaded edge of the gyroid using different distance metrics in the random field generation

the cumulative distribution function leads to a probability of $\frac{1}{1.3124 \cdot 10^{23}}$ and is not considered an issue in this analysis. For more significant standard deviations, a lognormal distribution would be more appropriate. The second-order estimate generated is directly affected by the distribution of the random-field variables. Switching distributions, therefore, results in different results in general. This study analyzes only the effects of geodesic vs. Euclidean distances, which is possible to do qualitatively using a Gaussian distribution.

4.1.2. Results

Geodesic distances computed differ significantly from Euclidean distances between points. Figure 9 illustrates this through a difference that reaches up to 25% for this example. Generating fields with this differing length and correlation matrix also leads to a different looking field. Figure 10 shows examples of fields generated using both distance metrics in the correlation function. Fields generated using a geodesic distance show more variation within the structure than fields using Euclidean distance.

Figure 11 shows the probability density function (pdf) of the displacement of both statistical analyses. Statistical properties of these distributions are shown in table 2.

Comparing the two analyses, it is clear that a significant deviation of the statistical properties can be present when the distance used for random field generation does not reflect the actual geodesic distance. This deviation depends on the actual structure (curvature and size), and the correlation function used to generate the fields.

4.2. Isotropic cylindrical shell with scalar variations

The second example analyzed deals with variations in thickness and Young's modulus in a cylinder. These results verify the implementation by comparing them with published results. Arbocz and Abramovich [85] published a series of geometric imperfection measurements of isotropic

Property	Value
E	Gaussian random field: $\mu = 104.41$ GPa $\sigma = 10.441$ GPa (CoV 10%) $L_c = 50-500$ mm
ν	0.3
Thickness	Gaussian random field: $\mu = 0.11597$ mm $\sigma = 0.011597$ mm (CoV 10%) $L_c = 50-500$ mm

Table 3: Material and thickness properties of the isotropic cylinder. **Note**: Young's modulus and thickness variations are not applied simultaneously. When one is applied as a random field, the mean value of the other is used as a deterministic value.

cylindrical shells referred to as the A-shells. The average property of shells A-7 to A-14 is often used in related imperfection analysis research. Imperfections that are analyzed are not just in nominal shape, but also local changes in thickness, Young's modulus, or a combination of these [86, 87, 88, 89]. Only the independent local variations of thickness and Young's modulus are analyzed independently within the current work.

4.2.1. Numerical analysis

The analyzed cylinder has a length of $L = 202.3$ mm, radius of $r = 101.6$ mm. Two series of analyses are performed in which either Young's modulus or the thickness is varied. When one is varied, the other is fixed to the mean value listed in table 3.

Using linear, curved shell elements, the cylinder is discretized into 213 circumferential elements and 67 axial, totaling 14271 elements. Using the coordinate system of fig. 12, the edge at $z = 0$ is constrained in all translations and rotation in the z-axis. At the edge $z = L$, translations in x and y directions are constrained, as well as rotations in the z-axis. Translations in the z-axis tied together on the top edge $z = L$, with distributed load is applied of -1.56649 N/m in the z-direction, giving a total of 1 N in compression. Results are normalized by the analytically obtained buckling load of the perfect cylinder calculated as

$$\lambda_{\text{analytical}} = \frac{2\pi E t^2}{\sqrt{3(1-\nu^2)}} = 5339 \text{ N}. \tag{34}$$

Variations are applied using the exponential correlation function of eq. (1), as well as the squared exponential function of eq. (2). A series of correlation lengths are used to generate Gaussian random fields ranging between 50-500 mm, the same range used by the study done by Papadopoulos and Papadrakakis [88] on this structure. Analyzing results over various correlation lengths makes it possible to identify the influence correlation lengths of imperfections have on the structure. Correlation lengths selected range from $\frac{L_c}{R} \approx 0.5$ to more large scale imperfections of $\frac{L_c}{R} \approx 5$. The standard deviation of the variations is 10% of the nominal value

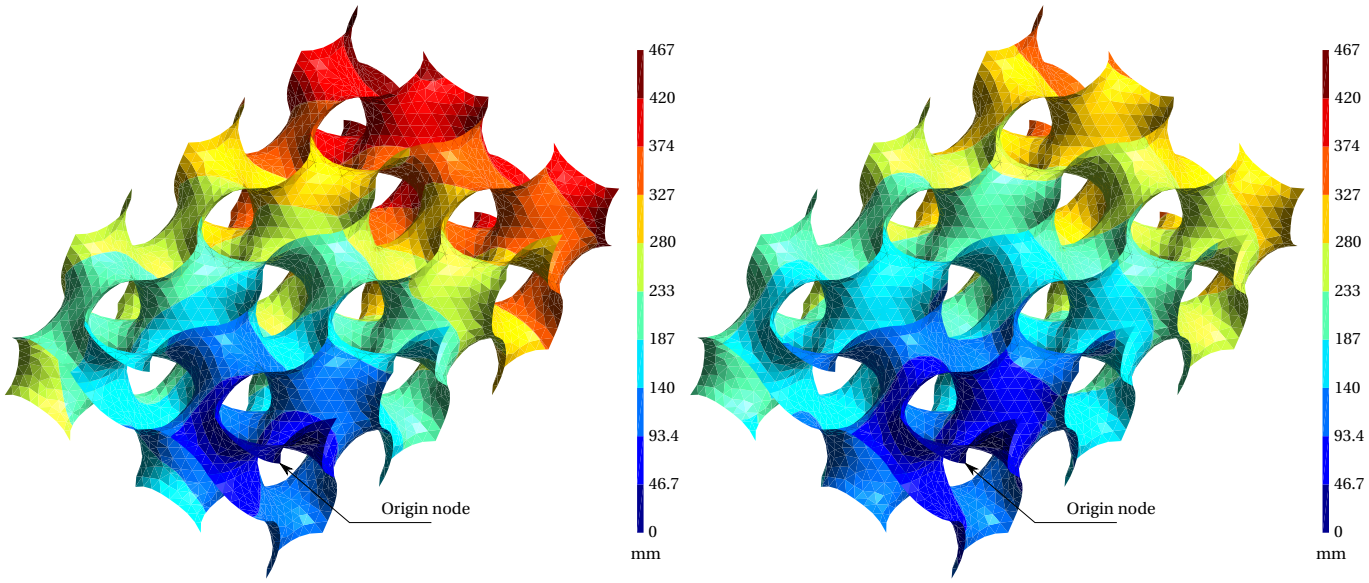

(a) Geodesic distance

(b) Euclidean distance

Figure 9: Distances computed from a corner of gyroid

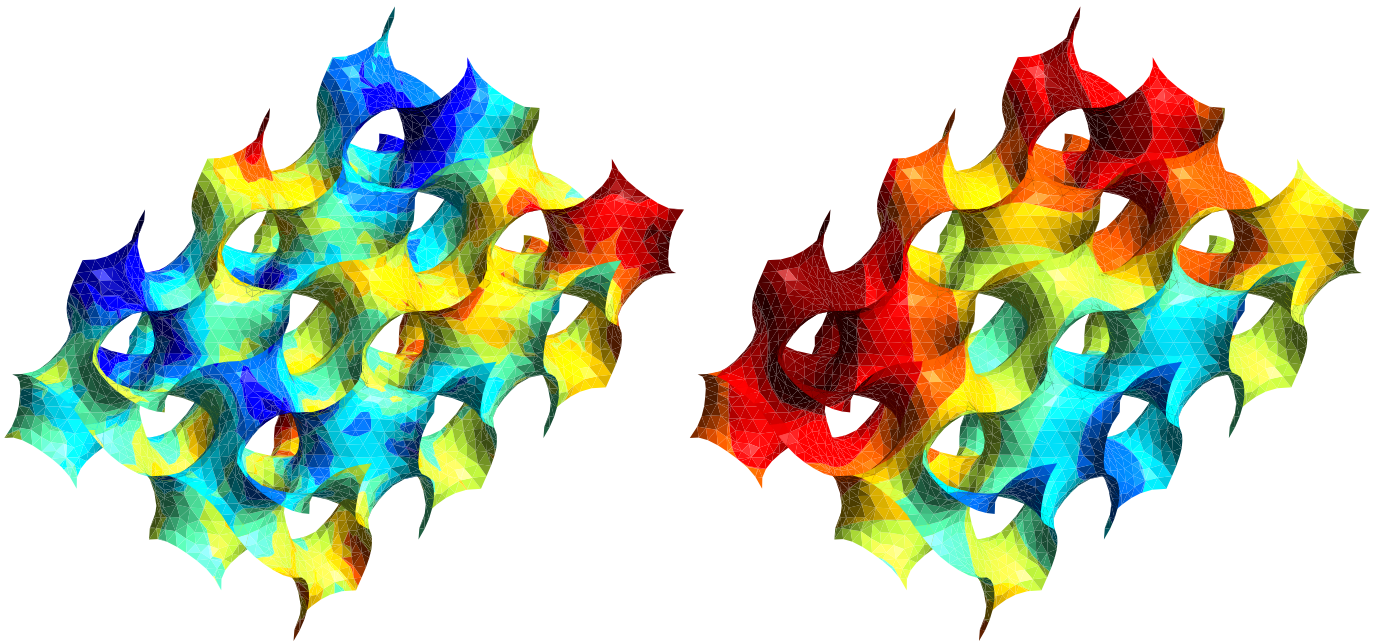

(a) Random field generated using geodesic distance

(b) Random field generated using Euclidean distance

Figure 10: Random fields generated using two different distance metrics and $L_c = 100$ mm

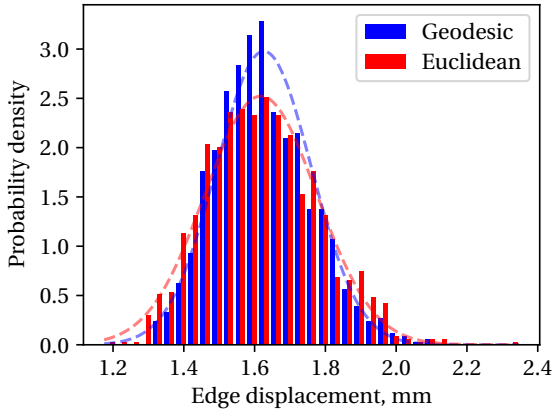

Figure 11: Displacement in x-direction of loaded edge (y=0) of the gyroid structure

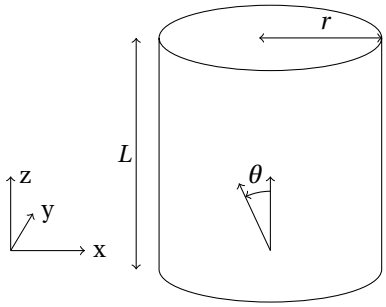

Figure 12: Cylinder geometry definition

of both the thickness and Young's modulus series of analyses. Although Gaussian fields can potentially result in non-physical values of Young's modulus and thickness, this is not an issue for this particular example [89, sec. 7.1]. However, analyses with larger variations should switch to a lognormal distribution or other distribution that guarantees positive values. Results in this analysis are directly compared with published results generated using a Gaussian distribution, making direct comparison possible. In the general case when experiments are reproduced, for instance, the distribution of the input variable has to be carefully reproduced to generate an estimate of the variance.

A series of 250 analyses were performed for every correlation length analyzed, the same amount as the referred paper. The convergence of statistical properties was checked qualitatively after the analysis and found to show reasonable convergence. The applied load is slowly increased during the geometrically non-linear analysis using a Newton-based approach until the tangential stiffness matrix contains a negative eigenvalue, meaning the bifurcation buckling load is reached.

4.2.2. Results

Results found in fig. 13 show the statistical properties of analyses that apply local Young's modulus or thickness variations. Fields generated in the referred literature [88] use

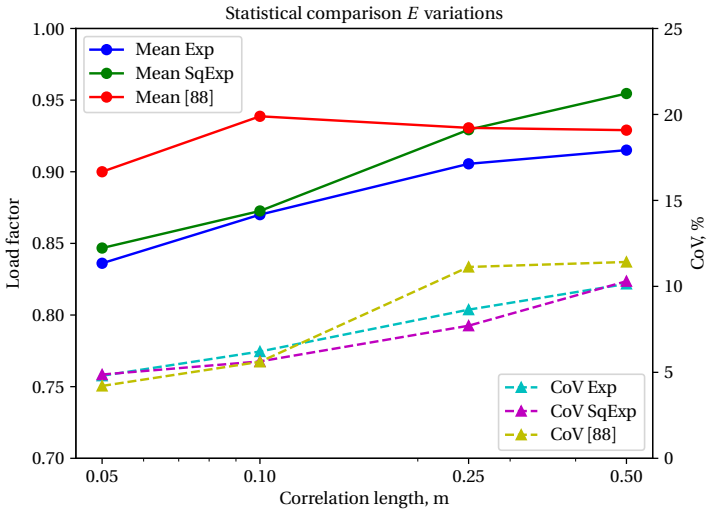

(a) Statistical properties of structures affected by local Young's modulus variations

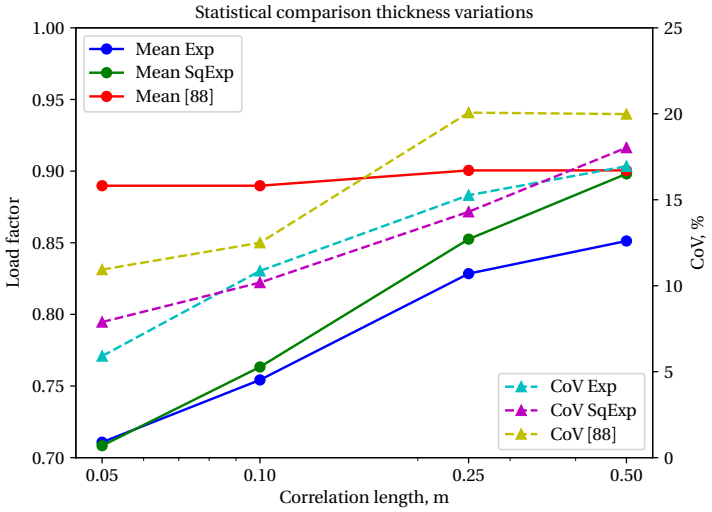

(b) Statistical properties of structures affected by local thickness variations

Figure 13: Statistical properties of the critical load factor of analyses run with random fields of varying correlation lengths affecting the local Young's modulus or thickness

a squared exponential correlation function. Overall, fields generated using the squared exponential correlation function show a higher mean value for the critical load, while the coefficient of variation ($\frac{\sigma}{\mu}$)is only slightly lower.

Verifying results generated with the current approach and those published by Papadopoulos and Papadrakakis [88], there is an apparent discrepancy in the mean value of the stochastic results. Lower correlation lengths result in a higher value for the buckling than those generated using the geodesic approach. Papadopoulos et al. were aware of the deviation between their modelâĂŹs results and results that are obtained using a considerably finer mesh. However, they asserted that such a deviation would be consistent in their stochastic results and not affect the stochastic response. This deviation was emphasized within the paper's geometric imperfections analysis, in which a 15% increase in mean buckling load was found compared to results from Schenk and Schuëller [86].

Checking this hypothesis was done by slowly refining the mesh for one particular configuration and analyzing the convergence of the stochastic results. Figure 14 shows the stochastic convergence of stochastic parameters of structures with imperfections applied with a square exponential correlation function and a 0.1 m correlation length. Comparing the mean buckling values of figs. 13 and 14, the mean normalized buckling load of the referred literature seems to be overestimated, corresponding to values obtained with a mesh in the order of 5000-8000 elements.

Comparing the coefficient of variation between the results shows a closer fit, particularly with Young's modulus variations. Stochastic results of the thickness varying analyses show a more significant deviation, however, not just in the variance but also in the mean value. The larger discrepancy is due to the additional refinement needed to properly evaluate the more significant change in local stiffness attributed to local thickness changes. Unlike the linear relationship with Young's modulus variations, thickness changes have a cubic relationship to bending stiffness. Such more distinctive gradients in bending stiffness require a more refined mesh to evaluate accurately, indicating that the assumption made in [88] is only valid when the stiffness gradients are not very large. Recent work from Feng et al. [56] reproduces the thickness variation example and shows a similar discrepancy compared to the original publication, with results being closer to those in the current work.

4.3. Waters' shell

Effects of fiber angle variations and geometric imperfections are demonstrated using a composite cylindrical shell. Dimensions and properties used are identical to the shell initially analyzed by Waters [90] and consequently used by other researchers, e.g. [91, 92, 93].

The cylinder is 355.6 mm tall with a 203.18603 mm radius, consisting of 8 layers with a total nominal thickness of 1.01539 mm with a $[\pm 45, 0, 90]_s$ layup. Material properties of the lamina can be found in table 4.

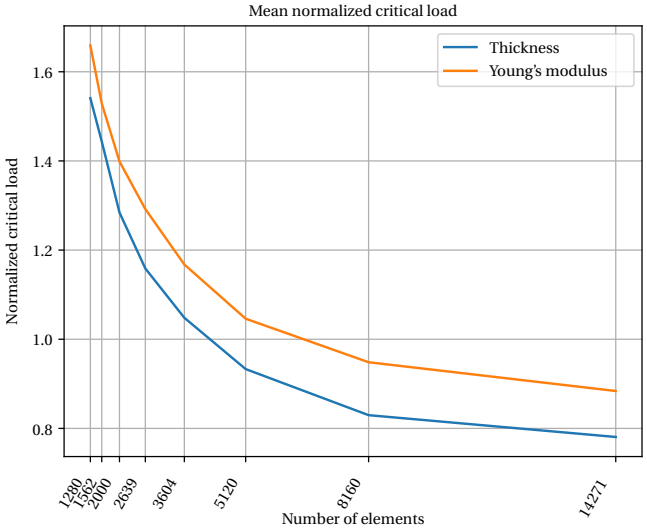

(a) Mean normalized buckling load computed with different mesh sizes

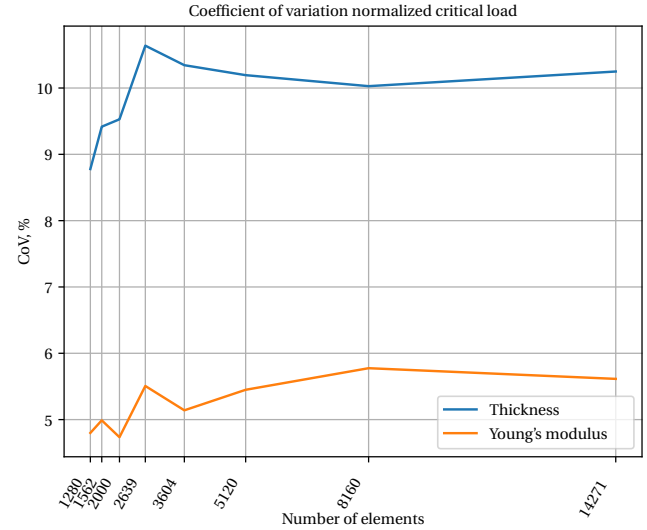

(b) Coefficient of variation of normalized buckling load computed with different mesh sizes

Figure 14: Convergence of statistical properties of the cylindrical shell with different mesh sizes under the influence of imperfections in thickness or Young's modulus. Fields applied are generated using a square exponential correlation function and correlation length of 0.1 m

Property	Value
E_1	127.629 GPa
E_2	11.3074 GPa
G_{12}	6.00257 GPa
ν_{12}	0.300235
Fiber misalignment of θ_i	Gaussian random fields:
$i \in [1 \dots 8]$	$\mu = 0°$
	$\sigma = 2°$
	$L_c = 50 - 500$ mm
Thickness	1.01539 mm

Table 4: Material properties of Water's composite shell [90] and stochastic parameters used for fiber misalignments

Top and bottom edges at $z = 0$ and $z = L$ in fig. 12 are constrained in the radial direction, leaving the axial direction free. One node on the bottom edge is constrained in the z direction to remove the rigid body mode. The cylinder is discretized into a mesh of 6536 analytically integrated triangular elements. Mesh is converged to reproduce buckling results published in [93, tab. 3.13]. Results obtained are normalized using the linear bucking load found for the perfect cylinder (without variations applied), which equals $\lambda_{lin} = 135.7$ N/mm.

This example aims to analyze the structure's geometrically non-linear behavior. Accurately representing the complex geometric behavior requires sufficient fidelity in the displacement field. Analyzing the criticality of geometric imperfections demands a displacement field to be accurate enough to represent a given imperfection pattern. The discretization has a mean element size of 12.7 mm. The amount of elements needed to represent a local variation depends on the correlation function, correlation length, and structure. A minimum of five elements over the correlation length is used within this analysis, meaning a minimum of 50 mm is used. 50 mm equals around 14% of the axial length and 4% of the circumference of the cylinder. Fields are generated using a Gaussian distribution, which closely matches imperfections found in real structures [77].

4.3.1. *Analysis of critical loads with fiber-misalignments applied*

Stochastic variations on the fiber layup are applied using Gaussian random fields with a standard deviation of $\theta_\sigma = 2°$. These imperfections are applied through fields generated over a range of correlation lengths, using the squared exponential correlation function (eq. (2)). The effects of anisotropic heat coefficients in calculating pseudo-distance calculations and inter-field correlation are discussed in section 2.3. Anisotropy in the distance measurements of the fields is achieved by applying $k_z = 50$ in the distance calculation. The z-axis is defined in fig. 12 as the axial direction of the cylinder. The inter-field correlation $\boldsymbol{\Sigma}$ used in the analyses are:

Equicorrelation, (cρ) All fields in a run have an equal correlation to one another,

$$\boldsymbol{\Sigma} = \begin{bmatrix} 1 & \rho & \rho & \dots & \rho \\ \rho & 1 & \rho & \dots & \rho \\ \vdots & \vdots & \vdots & \ddots & \vdots \\ \rho & \rho & \rho & \dots & 1 \end{bmatrix}, \tag{35}$$

where $\rho \in \begin{bmatrix} 0.3 & 0.5 & 0.9 \end{bmatrix}$, making all fields equally similar to each other. Such a series of fields suitable for modeling, for example, fiber imperfections which are influenced by curing in an equal manner between layers (for instance, in very thin structures).

Identity (I) All fields are completely independent from each other, $\boldsymbol{\Sigma} = I_8$. Generating a set of fields using an identity correlation matrix implies that fields are completely independent. This is equivalent to generating the fields separately without taking others into account.

Material gradient (mat) Fields in a structure are less correlated the more distance they have between them,

$$\boldsymbol{\Sigma} = \begin{bmatrix} 1.00 & 0.90 & 0.80 & 0.70 & 0.60 & 0.50 & 0.40 & 0.30 \\ 0.90 & 1.00 & 0.90 & 0.80 & 0.70 & 0.60 & 0.50 & 0.40 \\ 0.80 & 0.90 & 1.00 & 0.90 & 0.80 & 0.70 & 0.60 & 0.50 \\ 0.70 & 0.80 & 0.90 & 1.00 & 0.90 & 0.80 & 0.70 & 0.60 \\ 0.60 & 0.70 & 0.80 & 0.90 & 1.00 & 0.90 & 0.80 & 0.70 \\ 0.50 & 0.60 & 0.70 & 0.80 & 0.90 & 1.00 & 0.90 & 0.80 \\ 0.40 & 0.50 & 0.60 & 0.70 & 0.80 & 0.90 & 1.00 & 0.90 \\ 0.30 & 0.40 & 0.50 & 0.60 & 0.70 & 0.80 & 0.90 & 1.00 \end{bmatrix}, \tag{36}$$

meaning that the field of layer 1 is correlated by layer 2 with 0.9 for instance, but only 0.3 with layer 8. Using such a correlation structure could potentially take curing imperfections of fiber misalignments into account for thicker structures or structures with larger curvatures where curing effects vary through thickness.

Five hundred samples are computed for each of these runs. The critical load is defined as the limit point load in which a tangential stiffness matrix becomes singular. A Newton-Raphson solver is used to compute the critical load using automatic load-step resizing. The number of samples required was determined in a convergence study. This study involved performing 1000 analyses for a few different configurations and analyzing when the mean and standard deviation values stabilize.

4.3.2. *Results of stability analyses with fiber-misalignments applied*

A total of 45000 analyses were performed in 90 different configurations, as shown in figs. 15 and 16. Isotropic results, in which $k_x = k_y = k_z = 1$ have the correlation of points on a field directly coupled to the geodesic distance are shown in figs. 15a and 15b, with two example structures shown in figs. 18 and 19. Anisotropic results which use a pseudo-distance to generate correlation values are shown

in figs. 16a and 16b, with two example structures shown in figs. 20 and 21.

Results show that both the critical load and coefficient of variation vary significantly depending on the correlation length used. Mean critical load values go up as the correlation length increases. Physically these represent smoother and less local fiber angle variations.

The coefficient of variation of the results also varies significantly with the correlation length used. Values initially increase with the correlation length up to 75 mm for isotropic and 37.5 for anisotropic fields, after which the value drops to almost half of its peak value at 150-200 mm (isotropic) or 100-350 (anisotropic). It then goes up with increasing correlation length.

Comparing the isotropic and anisotropic fields, it is clear that a change in the critical correlation (pseudo-)length affects the results. Anisotropic fields generated have less variation in the axial direction. These more consistent variations can cause larger deviations from the axisymmetric deformation of an ideal cylinder, causing slightly lower buckling loads and more variation than the isotropic analyses.

Inter-field correlation has a significant effect on both the mean value and the coefficient of variation in the analyses performed. Overall the critical value decreases as fields become more independent while at the same time increasing the variance. An essential factor is that the quasi-isotropic layup of the structure can show more anisotropic behavior when fields vary independently. Behavior such as compression-twist coupling can have a more significant effect in such cases.

Variation in the results computed is limited, with a coefficient of variation below 2%. It is important to note that the results do illustrate that inter-correlation and correlation length both have a significant effect on the variance obtained. The amplitude of the resulting analyses can increase significantly when the amplitude of variations is increased, or if the structure being analyzed has unstable nonlinear paths for instance.

4.3.3. Analysis of critical loads with geometric imperfections applied

Geometric imperfections are also applied to the Waters shell using the procedure described in section 2.2.1. Geometric imperfections are applied with a standard deviation equal to $\sigma = 0.1t \approx 0.1$ mm from the nominal coordinate. This value is within the maximum range measured for a cylinder by NASA [94]. It should be noted that this value would likely differ in real structures depending on the length scale of variations, e.g., the correlation length. The same value is used for all analyses for the sake of consistency.

The analyses are solved the same way the fiber deviation analyses are, using a Newton-Raphson approach with automatic step resizing to find the structure's limit-point load.

4.3.4. Results of stability analyses with geometric imperfections applied

Figure 17 shows the statistical properties of geometrically imperfect analyses. The mean value's overall trends are similar to those of the fiber deviation, with a general increase in the correlation length. Variance, however, shows different behavior to that of fiber angle variations. There is a general decrease in the variance as the correlation length increases. Trends in the variance values are similar between the isotropic and anisotropic analyses, with values in the isotropic analyses being approximately 60-70% higher.

Imperfections representing the out-of-plane displacement use the same standard deviation for every correlation length. Therefore, shorter correlation lengths contain a higher degree of local curvature as the size of imperfections decreases, but the amplitudes remain the same.

Variance decreases with an increase in correlation length. As imperfections become more smoothed out and less localized, they are less likely to have an aggressive influence.

5. Discussion and conclusions

Adaption in finite elements of the heat method has dramatically simplified and accelerated the computation of geodesic random fields in structural mechanics. A random field is used to represent deviations from an ideal geometry or material property. A cylindrical shell is used to demonstrate the geodesic distance calculation. As the number of elements increases and the time step t decreases, the geodesic calculations converge to the exact analytical solution.

Substituting isotropic heat conductivity for anisotropic coefficients makes it possible to generate "pseudo-distances" scaled with the material orientation. These pseudo-distances lead to anisotropic fields, which can have an anisotropic correlation. Anisotropic fields can potentially better represent defects in specific structures introduced during manufacturing processes.

Compared to previous work done on geodesic random fields in structural analysis, the approach presented has the following benefits:

Speed Computationally, the approach to geodesic distance calculation is very efficient and scales almost linearly with the number of points evaluated. Compared to the exact "MMP" approach [54] used by Scarth et al. [53], the time to compute distances can easily be several orders of magnitude faster.

Anisotropy Anisotropy The MMP method only generates isotropic random fields, as the distances can not be scaled to generate a directional dependency. Changing the heat conductivity could also change the correlation length locally by scaling the computed "pseudo-distance", leading to non-stationary fields.

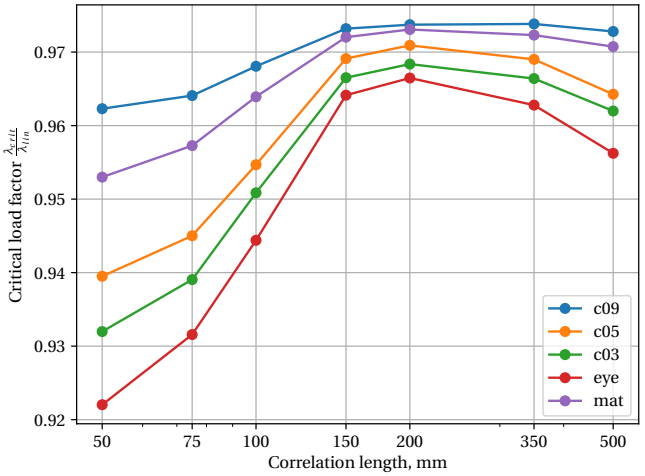

(a) Mean value of normalized critical buckling load of configuration with isotropic (geodesic) random fields with random fields of different correlation lengths

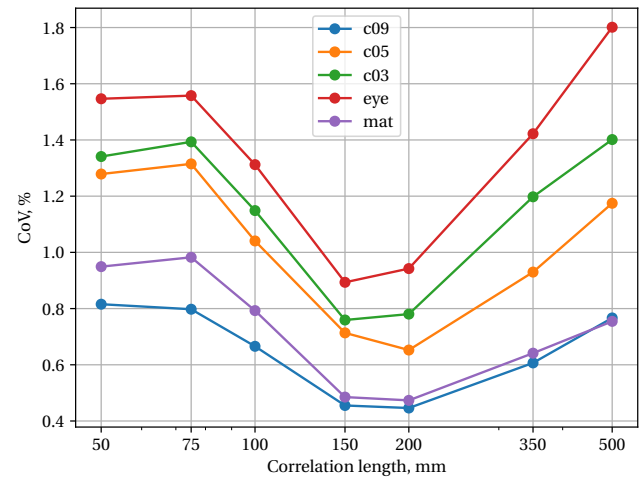

(b) Coefficient of variation of critical buckling load of configuration with isotropic (geodesic) random fields of different correlation lengths

Figure 15: Waters shell critical load λ_{crit} under fiber orientation variations of different correlation lengths, and different inter-layer correlation. Configurations mentioned in the legend are discussed in section 4.3.1. Correlations with a field use the geodesic distance generated using isotropic thermal conductivity in the geodesic distance calculation.

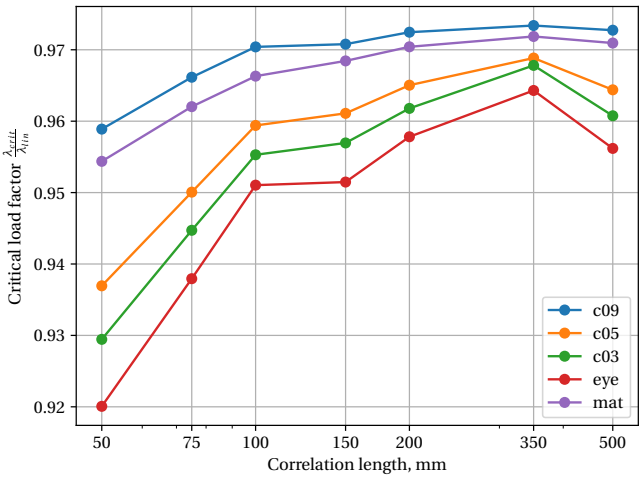

(a) Mean value of normalized critical buckling load of configuration with anisotropic random fields of different correlation lengths

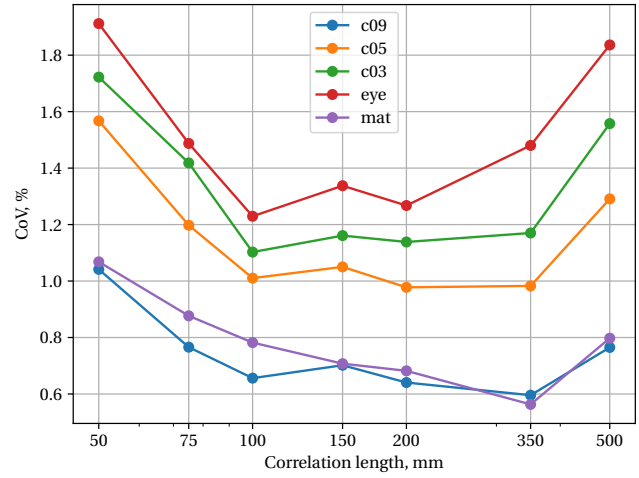

(b) Coefficient of variation of critical buckling load of configuration with anisotropic random fields of different correlation lengths

Figure 16: Waters shell critical load λ_{crit} under fiber orientation variations of different correlation lengths, and different inter-layer correlation. Configurations mentioned in the legend are discussed in section 4.3.1. Correlations with a field use the geodesic distance generated using anisotropic thermal conductivity in the geodesic distance calculation, creating pseudo-distances which are used in the correlation function.

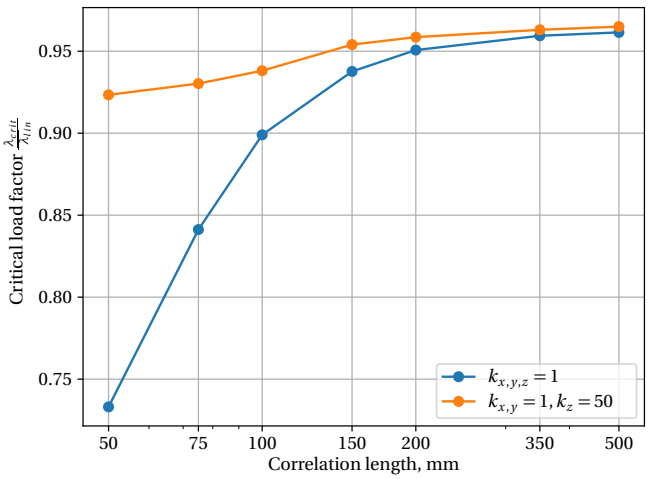

(a) Mean value

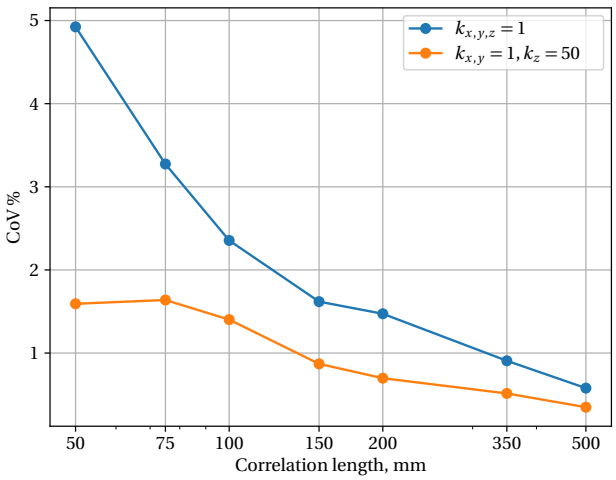

(b) Coefficient of variation

Figure 17: Waters shell critical load λ_{crit} with geometric imperfections of different correlation lengths. Distances used in the correlation length use either isotropic (leading to geodesic distances) or anisotropic (leading to pseudo-distances) thermal conductivity.

Element order The MMP method described in [54] can be used to compute geodesic distances on polyhedral surfaces. As a first step, the polyhedral has to be triangulated. Triangulation adds a step to the distance calculation (assuming the model does not use linear triangular shell elements) and limits the type and effective order of elements used. Elements that use higher-order shape functions have to be linearized locally, losing curvature information and accuracy.

Element type The approach presented is not limited to a specific element type. The numerical examples use shell elements, but the approach is also fully functional for bar, beam and solid elements. The more extensive element library makes it possible to accurately model structures or materials requiring different elements.

A few examples are used to demonstrate the approach in structural mechanics. The first example illustrates that it is vital to use geodesic distances when a structure has curvature. The spread of imperfections can cause significant discrepancies in results when substituted by correlations obtained with Euclidean distance. The gyroid example showed a discrepancy of 20% for end displacement under shear loading.

Replicating an example from literature in which Young's modulus and thickness vary in a cylindrical shell shows a potential source of error in computation. Structures susceptible to very local imperfections (e.g., structures with buckling modes with a short wavelength) need to be discretized and modeled in a sufficiently refined model to represent the mechanical behavior accurately. Therefore, mesh convergence studies should focus on the shortest correlation length of fields applied to a structure.

A final example analyzes the effect of local fiber misalignment. Both isotropic and anisotropic heat conductivity is used in the random field generation. Additionally, different types of correlation between layers of the composite are analyzed. These parameters both significantly influence the statistical response of a structure to imperfections.

Overall the approach presents a significant computational improvement in generating geodesic random fields. It uses existing capabilities found in finite element solvers to solve potential flow problems in the computation of geodesic distances, simplifying implementation. The generality of the formulation makes it possible to apply the approach to a variety of element types without any inherent limitations.

Acknowledgements

This project has received funding from the European Union's Horizon 2020 research and innovation program under the Marie Skłodowska-Curie grant agreement No. 642121.

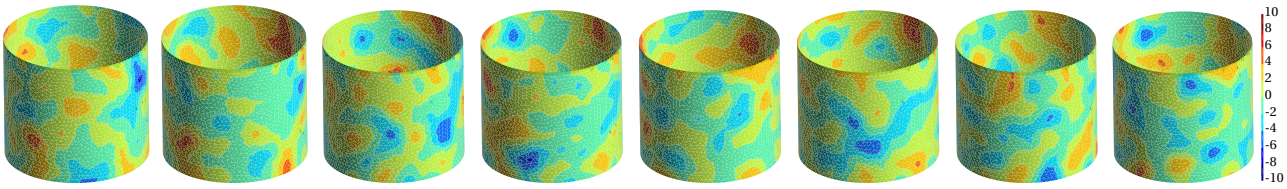

(a) Layer 1 (b) Layer 2 (c) Layer 3 (d) Layer 4 (e) Layer 5 (f) Layer 6 (g) Layer 7 (h) Layer 8

Figure 18: Degrees fiber deviation of fields generated with $L_c = 50$ mm, isotropic distance, and equal correlation to each other of $\rho = 0.5$ ($\rho 0.5$) per eq. (35)

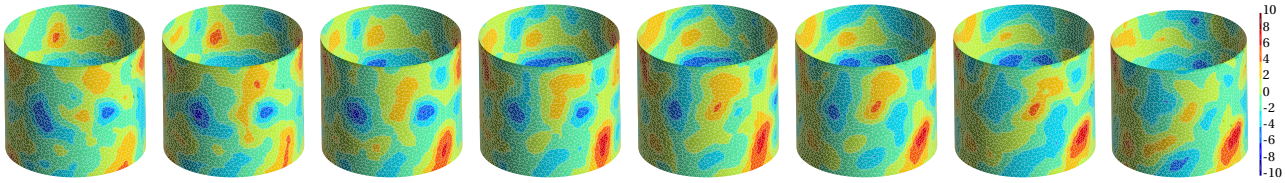

(a) Layer 1 (b) Layer 2 (c) Layer 3 (d) Layer 4 (e) Layer 5 (f) Layer 6 (g) Layer 7 (h) Layer 8

Figure 19: Degrees fiber deviation of fields generated with $L_c = 50$ mm, isotropic distance, and a field correlation that reduces with increasing distance between fields (mat) per eq. (36)

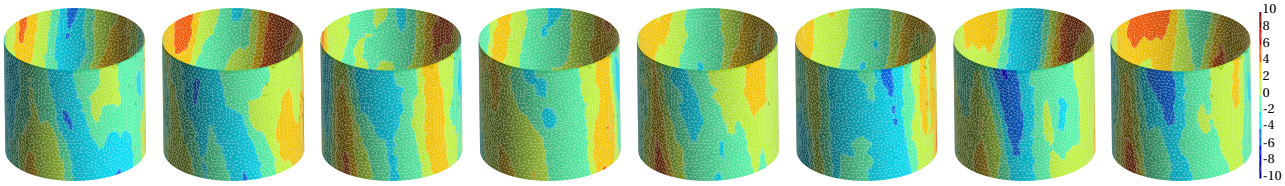

(a) Layer 1 (b) Layer 2 (c) Layer 3 (d) Layer 4 (e) Layer 5 (f) Layer 6 (g) Layer 7 (h) Layer 8

Figure 20: Degrees fiber deviation of fields generated with $L_c = 50$ mm, anisotropic ($k_x = 1, k_y = 50$) distance, and equal correlation to each other of $\rho = 0.5$ ($\rho 0.5$) per eq. (35)

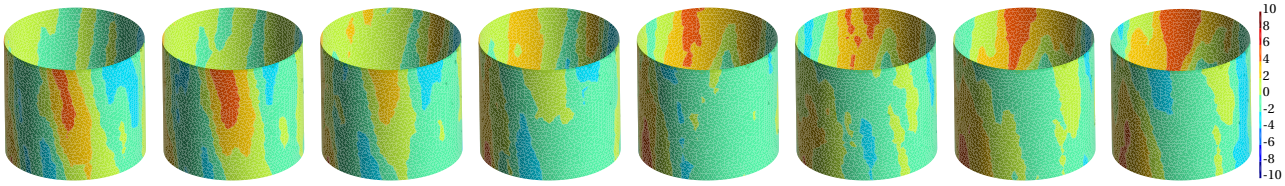

(a) Layer 1 (b) Layer 2 (c) Layer 3 (d) Layer 4 (e) Layer 5 (f) Layer 6 (g) Layer 7 (h) Layer 8

Figure 21: Degrees fiber deviation of fields generated with $L_c = 50$ mm, anisotropic ($k_x = 1, k_y = 50$) distance, and a field correlation that reduces with increasing distance between fields (mat) per eq. (36)

The authors would like to acknowledge the help of Gerd-Jan Schreppers and Tanvir Rahman of Diana FEA B.V. for their assistance in the numerical implementation within Diana, and for hosting one of the authors during a research stay.

References

[1] G. Stefanou, The stochastic finite element method: Past, present and future, Computer Methods in Applied Mechanics and Engineering 198 (2009) 1031–1051.

[2] R. G. Ghanem, P. D. Spanos, Stochastic Finite Elements: A Spectral Approach, Springer-Verlag New York, 1991.

[3] A. Der Kiureghian, J.-B. Ke, The stochastic finite element method in structural reliability, Probabilistic Engineering Mechanics 3 (1988) 83–91.

[4] B. Sudret, a. D. Kiureghian, Stochastic Finite Element Methods and Reliability: A State-of-the-Art Report, University of California Berkeley (2000) 189.

[5] P. Sasikumar, R. Suresh, P. K. Vijayaghosh, S. Gupta, Experimental characterisation of random field models for CFRP composite panels, Composite Structures 120 (2015) 451–471.

[6] S. Sriramula, M. K. Chryssanthopoulos, An experimental characterisation of spatial variability in GFRP composite panels, Structural Safety 42 (2013) 1–11.

[7] S. Sriramula, M. K. Chryssanthopoulos, Quantification of uncertainty modelling in stochastic analysis of FRP composites, Composites Part A: Applied Science and Manufacturing 40 (2009) 1673–1684.

[8] L. Junyan, L. Liqiang, W. Yang, Experimental study on active infrared thermography as a NDI tool for carbon-carbon composites, Composites Part B: Engineering 45 (2013) 138–147.

[9] D. Saenz-Castillo, M. Martín, S. Calvo, F. Rodriguez-Lence, A. Güemes, Effect of processing parameters and void content on mechanical properties and NDI of thermoplastic composites, Composites Part A: Applied Science and Manufacturing 121 (2019) 308–320.

[10] A. Manta, M. Gresil, C. Soutis, Infrared thermography for void mapping of a graphene/epoxy composite and its full-field thermal simulation, Fatigue and Fracture of Engineering Materials and Structures (2019) 1–13.

[11] E. H. Vanmarcke, Random Fields: Analysis and Synthesis, The MIT Press, 1983.

[12] P. D. Spanos, B. A. Zeldin, Monte Carlo Treatment of Random Fields: A Broad Perspective, Applied Mechanics Reviews 51 (1998) 219.

[13] G. A. Fenton, Simulation and Analysis of Random Fields, Ph.D. thesis, 1990.

[14] D. Hristopulos, Random Fields for Spatial Data Modeling, Springer Nature B.V., 2020.

[15] P. D. Spanos, R. G. Ghanem, Stochastic Finite element expansion for random media, Journal of Engineering Mechanics 115 (1989) 1035–1053.

[16] W. Betz, I. Papaioannou, D. Straub, Numerical methods for the discretization of random fields by means of the Karhunen-Loeve expansion, Computer Methods in Applied Mechanics and Engineering 271 (2014) 109–129.

[17] B. Kriegesmann, R. Rolfes, C. Hühne, J. Teßmer, J. Arbocz, Probabilistic Design of Axially Compressed Composite Cylinders With Geometric and Loading Imperfections, International Journal of Structural Stability and Dynamics 10 (2010) 623–644.

[18] M. W. Davis, Production of conditional simulations via the LU triangular decomposition of the covariance matrix, Mathematical Geology 19 (1987) 91–98.

[19] M. Shinozuka, G. Deodatis, Simulation of multi-dimensional Gaussian stochastic fields by spectral representation, Applied Mechanics Reviews 49 (1996) 29–53.

[20] G. A. Fenton, E. H. Vanmarcke, Simulation of Random Fields via Local Average Subdivision, Journal of Engineering Mechanics 116 (1990) 1733–1749.

[21] S. van den Broek, S. Minera, A. Pirrera, P. M. Weaver, E. Jansen, R. Rolfes, Enhanced deterministic performance of panels using stochastic variations of geometry and material, AIAA Journal 58 (2020) 2307–2320.

[22] C.-C. Li, A. Der Kiureghian, Optimal discretization of random fields, Journal of engineering mechanics 119 (1993) 1136–1154.

[23] E. Vanmarcke, M. Grigoriu, Stochastic Finite Element Analysis of Simple Beams, Journal of Engineering Mechanics 109 (1983) 1203–1214.

[24] B. Kriegesmann, R. Rolfes, E. L. Jansen, I. Elishakoff, C. Hühne, A. Kling, Design optimization of composite cylindrical shells under uncertainty, Computers, Materials and Continua 32 (2012) 177–200.

[25] J. Zhao, C. Wang, Robust structural topology optimization under random field loading uncertainty, Structural and Multidisciplinary Optimization 50 (2014) 517–522.

[26] E. Bielewicz, J. Górski, Shells with random geometric imperfections simulation - Based approach, International Journal of Non-Linear Mechanics 37 (2002) 777–784.

[27] G. Chen, H. Zhang, K. J. Rasmussen, F. Fan, Modeling geometric imperfections for reticulated shell structures using random field theory, Engineering Structures 126 (2016) 481–489.

[28] C. C. Bienstock, J. T. Mentzer, The use of Response Surface Methodology Estimation of Composite Engineering Structures 16 (1995) 197–226.

[29] E. Bielewicz, J. Górski, R. Schmidt, H. Walukiewicz, Random fields in the limit analysis of elastic-plastic shell structures, Computers and Structures 51 (1994) 267–275.

[30] S. Lauterbach, M. Fina, W. Wagner, Influence of stochastic geometric imperfections on the load-carrying behaviour of thin-walled structures using constrained random fields, Computational Mechanics 62 (2018) 1107–1125.

[31] I. Vryzidis, G. Stefanou, V. Papadopoulos, Stochastic stability analysis of steel tubes with random initial imperfections, Finite Elements in Analysis and Design 77 (2013) 31–39.

[32] M. Fina, P. Weber, W. Wagner, Polymorphic uncertainty modeling for the simulation of geometric imperfections in probabilistic design of cylindrical shells, Structural Safety 82 (2020) 101894.

[33] M. Fina, L. Panther, P. Weber, W. Wagner, Shell Buckling With Polymorphic Uncertain Surface Imperfections and Sensitivity Analysis, ASCE-ASME Journal of Risk and Uncertainty in Engineering Systems, Part B: Mechanical Engineering 7 (2021).

[34] C. A. Schenk, G. I. Schuëller, Buckling analysis of cylindrical shells with cutouts including random boundary and geometric imperfections, Computer Methods in Applied Mechanics and Engineering 196 (2007) 3424–3434.

[35] Y. Luo, J. Zhan, P. Liu, Buckling assessment of thin-walled plates with uncertain geometrical imperfections based on non-probabilistic field model, Thin-Walled Structures 145 (2019) 106435.

[36] H. Wang, J. Guilleminot, B. W. Schafer, M. Tootkaboni, Stochastic analysis of geometrically imperfect thin cylindrical shells using topology-aware uncertainty models, Computer Methods in Applied Mechanics and Engineering 393 (2022) 114780.

[37] A. Pagani, A. R. Sanchez-Majano, Stochastic stress analysis and failure onset of variable angle tow laminates affected by spatial fibre variations, Composites Part C: Open Access 4 (2021) 100091.

[38] S. van den Broek, S. Minera, E. Jansen, R. Rolfes, Robust improvement of the asymmetric post-buckling behavior of a composite panel by perturbing fiber paths, Composite Structures 270 (2021) 114011.

[39] S. Shang, G. J. Yun, Stochastic finite element with material uncertainties: Implementation in a general purpose simulation program, Finite Elements in Analysis and Design 64 (2013) 65–78.

[40] V. Papadopoulos, D. C. Charmpis, M. Papadrakakis, A computationally efficient method for the buckling analysis of shells with stochastic imperfections, Computational Mechanics 43 (2009) 687–700.

[41] L. Graham, E. Siragy, Stochastic finite-element analysis for elastic buckling of stiffened panels, Journal of Engineering Mechanics 127 (2001) 91–97.

[42] J. Kepple, M. T. Herath, G. Pearce, B. Gangadhara Prusty, R. Thomson, R. Degenhardt, Stochastic analysis of imperfection sensitive unstiffened composite cylinders using realistic imperfection models, Composite Structures 126 (2015) 159–173.

[43] N. D. Lagaros, V. Papadopoulos, Optimum design of shell structures with random geometric, material and thickness imperfections, International Journal of Solids and Structures 43 (2006) 6948–6964.

[44] A. P. Teixeira, C. G. Soares, Ultimate strength of plates with random fields of corrosion, in: Structure and Infrastructure Engineering, volume 4, pp. 363–370.
[45] S. van den Broek, J. Wolff, S. Scheffler, C. Hühne, R. Rolfes, Improving the fatigue life of printed structures using stochastic variations, Progress in Additive Manufacturing (2022).
[46] A. Johari, A. Sabzi, A. Gholaminejad, Reliability Analysis of Differential Settlement of Strip Footings by Stochastic Response Surface Method, Iranian Journal of Science and Technology - Transactions of Civil Engineering 43 (2019) 37–48.
[47] A. Johari, A. Talebi, Stochastic Analysis of Piled-Raft Foundations Using the Random Finite-Element Method, International Journal of Geomechanics 21 (2021) 04021020.
[48] A. Johari, A. Heydari, Reliability analysis of seepage using an applicable procedure based on stochastic scaled boundary finite element method, Engineering Analysis with Boundary Elements 94 (2018) 44–59.
[49] A. Johari, A. Talebi, Stochastic Analysis of Rainfall-Induced Slope Instability and Steady-State Seepage Flow Using Random Finite-Element Method, International Journal of Geomechanics 19 (2019) 04019085.
[50] A. Johari, H. Fooladi, Comparative study of stochastic slope stability analysis based on conditional and unconditional random field, Computers and Geotechnics 125 (2020) 103707.
[51] H. Zhang, J. Guilleminot, L. J. Gomez, Stochastic modeling of geometrical uncertainties on complex domains, with application to additive manufacturing and brain interface geometries, Computer Methods in Applied Mechanics and Engineering 385 (2021) 114014.
[52] K. Crane, M. Livesu, E. Puppo, Y. Qin, A Survey of Algorithms for Geodesic Paths and Distances 1 (2020).
[53] C. Scarth, S. Adhikari, P. H. Cabral, G. H. C. Silva, A. P. d. Prado, P. Higino, G. H. C. Silva, A. P. d. Prado, Random field simulation over curved surfaces : Applications to computational structural mechanics, Computer Methods in Applied Mechanics and Engineering 345 (2019) 283–301.
[54] J. S. Mitchell, D. M. Mount, C. H. Papadimitriou, The Discrete Geodesic Problem, SIAM Journal on Computing 16 (1987) 647–668.
[55] E. W. Dijkstra, A note on two problems in connexion with graphs, Numerische Mathematik 1 (1959) 269–271.
[56] D. C. Feng, Y. P. Liang, X. Ren, J. Li, Random fields representation over manifolds via isometric feature mapping-based dimension reduction, Computer-Aided Civil and Infrastructure Engineering 37 (2022) 593–611.
[57] Y. P. Liang, X. Ren, D. C. Feng, Efficient stochastic finite element analysis of irregular wall structures with inelastic random field properties over manifold, Computational Mechanics 69 (2022) 95–111.
[58] K. Crane, C. Weischedel, M. Wardetzky, The Heat Method for Distance Computation, Communications of the ACM 60 (2017) 90–99.
[59] E. Del Castillo, B. M. Colosimo, S. D. Tajbakhsh, Geodesic gaussian processes for the parametric reconstruction of a free-form surface, Technometrics 57 (2015) 87–99.
[60] G. Christakos, D. T. Hristopulos, P. Bogaert, On the physical geometry concept at the basis of space/time geostatistical hydrology, Advances in Water Resources 23 (2000) 799–810.
[61] E. Anderes, J. Møller, J. G. Rasmussen, Isotropic covariance functions on graphs and their edges, Annals of Statistics 48 (2020) 2478–2503.
[62] M. A. Oliver, Modern spatiotemporal geostatistics, volume 108, 2002.
[63] P. Blanchard, O. Coulaud, E. Darve, Fast hierarchical algorithms for generating Gaussian random fields, Technical Report, Inria Bordeaux Sud-Ouest, 2015.
[64] M. Schevenels, B. S. Lazarov, O. Sigmund, Robust topology optimization accounting for spatially varying manufacturing errors, Computer Methods in Applied Mechanics and Engineering 200 (2011) 3613–3627.
[65] N. Wiener, Generalized harmonic analysis, Acta Math. 55 (1930) 117–258.
[66] S. R. S. Varadhan, On the behavior of the fundamental solution of the heat equation with variable coefficients, Communications on Pure and Applied Mathematics 20 (1967) 431–455.
[67] Diana FEA, DIANA Finite Element Analysis User's Manual Release 10.4, Technical Report, Delft, the Netherlands, 2020.
[68] R. D. Cook, D. S. Malkus, M. E. Plesha, R. J. Witt, Concepts and applications of finite element analysis, volume 4, Wiley New York, fourth edition, 2002.
[69] K. Crane, C. Weischedel, M. Wardetzky, Geodesics in heat: A new approach to computing distance based on heat flow, ACM Transactions on Graphics 32 (2013).
[70] F. M. Dekking, C. Kraaikamp, H. P. Lopuhaä, L. E. Meester, A Modern Introduction to Probability and Statistics: Understanding why and how, Springer Science & Business Media, 2005.
[71] M. Vořechovský, D. Novák, Simulation of random fields for stochastic finite element analysis, Icossar (2005) 2545–2552.
[72] P. Joubert, S. Langdell, Fixing a broken correlation matrix, 2019.
[73] R. Berger, B. Hofmeister, C. G. Gebhardt, R. Rolfes, A two-objective design optimisation approach for blending repairs of damaged compressor blisks, Aerospace Science and Technology 105 (2020) 106022.
[74] V. Papadopoulos, G. Soimiris, M. Papadrakakis, Buckling analysis of I-section portal frames with stochastic imperfections, Engineering Structures 47 (2013) 54–66.
[75] D. Schillinger, V. Papadopoulos, M. Bischoff, M. Papadrakakis, Buckling analysis of imperfect I-section beam-columns with stochastic shell finite elements, Computational Mechanics 46 (2010) 495–510.
[76] F. Yang, L. D. Cohen, Geodesic Distance and Curves Through Isotropic and Anisotropic Heat Equations on Images and Surfaces, Journal of Mathematical Imaging and Vision 55 (2016) 210–228.
[77] K. Sepahvand, Spectral stochastic finite element vibration analysis of fiber-reinforced composites with random fiber orientation, Composite Structures 145 (2016) 119–128.
[78] J. W. Harris, H. Stöcker, Handbook of mathematics and computational science, Springer Science & Business Media, 1998.
[79] R. P. Brent, Algorithms for minimization without derivatives, Courier Corporation, 2013.
[80] A. H. Schoen, Infinite periodic minimal surfaces without self-intersections, Nasa Technical Note D-5541 (1970) 92.
[81] Z. Qin, G. S. Jung, M. J. Kang, M. J. Buehler, The mechanics and design of a lightweight three-dimensional graphene assembly, Science Advances 3 (2017) 1–9.
[82] R. Tino, M. Leary, A. Yeo, M. Brandt, T. Kron, Gyroid structures for 3D-printed heterogeneous radiotherapy phantoms, Physics in Medicine and Biology 64 (2019) 0–11.
[83] D. Li, W. Liao, N. Dai, G. Dong, Y. Tang, Y. M. Xie, Optimal design and modeling of gyroid-based functionally graded cellular structures for additive manufacturing, CAD Computer Aided Design 104 (2018) 87–99.
[84] J. Podroužek, M. Marcon, K. Ninčević, R. Wan-Wendner, Bio-inspired 3D infill patterns for additive manufacturing and structural applications, Materials 12 (2019) 1–12.
[85] J. Arbocz, H. Abramovich, The initial imperfection data bank at the Delft University of Technology: Part I, 1979.
[86] C. A. Schenk, G. I. Schuëller, Buckling analysis of cylindrical shells with random geometric imperfections, International Journal of Non-Linear Mechanics 38 (2003) 1119–1132.
[87] V. Papadopoulos, P. Iglesis, The effect of non-uniformity of axial loading on the buckling behaviour of shells with random imperfections, International Journal of Solids and Structures 44 (2007) 6299–6317.
[88] V. Papadopoulos, M. Papadrakakis, The effect of material and thickness variability on the buckling load of shells with random initial imperfections, Computer Methods in Applied Mechanics and Engineering 194 (2005) 1405–1426.
[89] V. Papadopoulos, G. Stefanou, M. Papadrakakis, Buckling analysis of imperfect shells with stochastic non-Gaussian material and thickness properties, International Journal of Solids and Structures 46 (2009) 2800–2808.
[90] W. A. Waters, Effects of initial geometric imperfections on the behavior of graphite-epoxy cylinders loaded in compression, 1996.
[91] J. Arbocz, J. H. Starnes, M. P. Nemeth, On a high-fidelity hierarchical approach to buckling load calucations, 19th AIAA Applied Aerodynamics Conference (2001).
[92] B. Kriegesmann, E. L. Jansen, R. Rolfes, Design of cylindrical shells using the Single Perturbation Load Approach - Potentials and application limits, Thin-Walled Structures 108 (2016) 369–380.
[93] T. Rahman, A perturbation approach for geometrically nonlinear structural analysis using a general purpose finite element code, Ph.D.

thesis, Delft University of Technology, 2009.
[94] M. W. Hilburger, M. P. Nemeth, Shell Buckling Design Criteria Based on Manufacturing Imperfection Signatures, AIAA Journal 44 (2006) 654–663.